Iteratively comparing gravitational-wave observations to the evolution of massive stellar binaries

V. Delfavero,[1,2,*] R. O'Shaughnessy,[2] K. Belczynski,[3] P. Drozda,[4] and D. Wysocki[5]

[1]*Gravitational Astrophysics Laboratory, NASA Goddard Space Flight Center, Greenbelt, Maryland 20771, USA*

[2]*Center for Computational Relativity and Gravitation, Rochester Institute of Technology, Rochester, New York 14623, USA*

[3]*Nicolaus Copernicus Astronomical Center, Polish Academy of Sciences, ulica Bartycka 18, 00-716 Warsaw, Poland*

[4]*Astronomical Observatory, Warsaw University, Aleje Ujazdowskie 4, 00-478 Warsaw, Poland*

[5]*Department of Physics, University of Wisconsin–Milwaukee, Milwaukee, Wisconsin 53201, USA*

(Received 28 March 2023; accepted 29 June 2023; published 22 August 2023)

Gravitational-wave observations have the capability to strongly differentiate between different assumptions for how binary compact objects form. The agreement of observations to different models of the evolution of massive stellar binaries leading to the formation of compact binaries can be characterized by a Bayesian marginal likelihood. In this work, we show how to carefully interpolate this marginal likelihood between choices of binary evolution model parameters, enabling the analysis of their posterior distributions between expensive binary evolution simulations. Using the StarTrack binary evolution code, we compare one- and four-dimensional binary evolution models to the compact binary mergers reported in recent gravitational-wave observing runs, considering merger detection rates and mass distributions. We demonstrate that the predicted detection rates and mass distribution of simulated binaries can be effective in constraining binary evolution formation. We first consider a one-dimensional model, studying the effect of supernova (SN) kick velocity (drawn from a Maxwellian with dispersion $\sigma_{\rm eff}$) on the simulated population of compact binary mergers, and find support for substantial SN recoil kicks. We follow this up with a four-dimensional study of $\sigma_{\rm eff}$, mass transfer efficiency (f_a), the efficiency of angular momentum depletion from ejected material (β) during Roche-lobe accretion, and an observation-driven reduction in the mass-loss rate estimated from stellar wind models ($f_{\rm wind1}$). Of those four formation parameters we investigated, we find that three of them ($\sigma_{\rm eff}$, f_a, and $f_{\rm wind1}$) can be efficiently limited by these observational comparisons. After initially sampling from a uniform prior in the space of these parameters, we refined our sampling by iteratively estimating a Bayesian likelihood for each simulation, fitting that likelihood to a parametric model (a truncated Gaussian) in the four-dimensional formation parameter space, and sampling directly from that Gaussian in order to propose new simulations in a way that is informed by previous simulations. Our maximum likelihood simulation (K0559) has parameters $\sigma_{\rm eff} = 108.3$ km/s (indicating substantial SN recoil kicks), $f_a = 0.922$ (indicating efficient mass transfer), and $f_{\rm wind1} = 0.328$ (indicating support for reduced wind-driven mass loss). Note that our estimates are only valid within one particular model of compact binary formation through isolated binary evolution and do not yet take into account the impact of other uncertain pieces of stellar physics and binary evolution.

DOI: 10.1103/PhysRevD.108.043023

I. INTRODUCTION

By identifying and characterizing the properties of systems that become the observed gravitational-wave (GW) sources, the distribution of those properties in the population of coalescing compact binaries can now be measured empirically [1–9]. The first observation of gravitational-waves from the binary black hole (BBH) system, GW150914 [10], has quickly challenged candidate models for how these compact objects form. The discovery of this system demonstrated that black holes heavier than those observed in x-ray binaries exist [11], eliminating models that do not produce them. Similarly, the observation of the binary neutron star (BNS) and neutron star–black hole (NSBH) systems such as GW170817 [12], GW200105, and GW200115 [13], further define the population of these objects, which must be produced from the massive stars that become compact objects. The discoveries of GW190412 [14] and GW190814 [15] (with mass ratios $m_2/m_1 = 0.28^{+0.12}_{-0.06}$ and $0.112^{+0.008}_{-0.009}$,

*vera.delfavero@nasa.gov

respectively) similarly demonstrated that asymmetric binaries must be produced, eliminating models that cannot produce a wide mass ratio spectrum [13,16–20]. The population of gravitational-wave signals from coalescing compact binaries has an immediate impact on our understanding of the evolutionary tracks available to massive stellar binaries, even with the modest assumption that binary stellar astrophysical processes dominate at least some key parts of the observed compact binary distribution.

The formation channels for compact binaries include the isolated evolution of massive stellar binaries, isolated stellar triples, and dynamic mergers in dense environments such as near galactic nuclei, globular clusters, and dense star clusters (see Mandel and Farmer [21] for a review). Several theories postulate that many of the mergers observed thus far by modern ground-based gravitational-wave detectors can be explained by isolated binary evolution [19,22–33]. Others have argued that dynamic mergers are necessary to explain some events (like GW190521) [2,3,34–37]. In this work, we assume that the collective population of compact object mergers was formed through isolated binary evolution and reserve the inclusion of dynamic channels for future work.

Many groups have undertaken the pertinent task of modeling and simulating the evolution of massive isolated stellar binaries to construct simulated populations of mergers to compare with observations [38–51]. Previous studies with synthetic data have suggested direct comparisons with binary evolution catalogs could constrain binary evolution model parameters [52]. These models depend on assumptions about the life and evolution of stellar binaries, which vary from group to group and simulation to simulation, and include (but are not limited to) supernova shock propagation, pair instability, stellar wind, mass transfer, and metallicity. In this work, we will refer to the specific binary evolution model parameters varied from one simulation to the next as formation parameters Λ. Comparing any individual, detailed model for compact binary formation to observations is straightforward: the number of detections and properties of each event seen in a particular GW survey are compared quantitatively to the population of simulated mergers for a given model of binary evolution by a conventional (inhomogeneous Poisson process, marginalized) likelihood [1,53–56]. Simulating these populations incurs a high computational cost, severely limiting the ability to thoroughly explore the parameter space. In limited cases, pioneering studies have used postprocessing to implement single low-dimensional models that vary a handful of parameters at a time, for example, changing the spin distribution [54] or modifying the relative proportions (mixing fractions) between two fiducial reference models [57,58]. To surmount this challenge, some groups have created surrogate models for costly models like binary star evolution [53,59,60], allowing them to make continuous predictions for some parameter distributions as a function of some formation parameters.

Recently, some groups have begun to undertake the task of considering more than one set of model assumptions at once [28], however, they stop short of doing inference to interpolate between costly simulations and select new model parameter choices for further simulations. In practice, however, these complex models have many parameters and are undergoing tremendous developments that can dramatically impact their predictions, such as the choice for supernova engine, remnant spins, and common-envelope (CE) assumptions. It would be difficult for these approximations to stay current and incorporate all relevant model physics or parameters.

In this work, we introduce a strategy to allow inference on compact binary formation models, without requiring continuously sampled models. Motivated by highly successfully strategies to interpret individual GW observations [61], we propose interpolating the marginalized likelihood over formation parameters and performing a Bayesian inference in these formation parameters. In this study, we vary formation parameters for supernova (SN) recoil kicks ($\sigma_{\rm eff}$), mass transfer efficiency during Roche-lobe overflow (f_a), specific angular momentum of material ejected during Roche-lobe overflow (β) [62], and a reduction in wind mass-loss rates for hydrogen-dominated stars ($f_{\rm wind1}$). Here, $\sigma_{\rm eff}$ is the dispersion parameter of a Maxwellian distribution. We compare GW observations from the first three observing runs of the LIGO/Virgo instruments [63–66] to models produced by the StarTrack binary evolution suite. Coupled with a range of postprocessing tools, the StarTrack suite produces merger rate densities for a population of compact binaries formed over cosmological time, accounting for a distribution of star forming conditions at each formation redshift [24,26,67–70].

Astrophysical interpretation relies on the joint likelihood $\mathrm{P}(\{d_j\}|\Lambda)$ of some specific model (with parameters Λ) given the data ($\{d_j\}$, consisting of individual confident detections: d_j). The Poisson likelihood, selection biases, observation results, and astrophysical inputs needed to carry out this program are readily available and well understood [71–74]. Several groups have already demonstrated how to use the likelihood of individual discrete models to discriminate between them [53,54,57]. However, at present, this approach remains tightly limited by model availability: the event rate as a function of formation parameters is only available for a very small set of population model parameters.

We organize the paper as follows. Section II reviews all the methods used in this work. First, in Sec. II A, we review the StarTrack binary evolution code, our binary evolution assumptions, and the range of binary evolution parameters explored by models used for inference in this study. Next, in Sec. II B, we review how we incorporate GW detector sensitivity to assess the properties of observed populations,

carefully describing how our calculations use the StarTrack binary evolution code. We specifically describe the fiducial detector network sensitivity estimate (i.e., the adopted detector noise power spectrum and signal-to-noise threshold for detection) adopted for the rest of this work. Subsequently, in Sec. II C, we describe how we evaluate the marginal likelihood of each model, as compared to gravitational-wave observations. Section III demonstrates our approach to binary population inference, in the context of a simple one-parameter investigation of SN recoil kick velocity. This section and the next compare observations from the first three observing runs of the LIGO/Virgo instruments to population models. Section IV applies these techniques to draw conclusions on the four formation parameters we explore in this study: f_a, β, $\sigma_{\rm eff}$, and $f_{\rm wind1}$. Finally, Sec. V discusses the implications of our results in the field of binary evolution population synthesis.

II. METHODS

A. StarTrack simulated universes

StarTrack binary evolution results have been exhaustively discussed before, both in isolation [25,67–70,75–77] and in comparison with GW observations [16,25,26,54,70,78]. O'Shaughnessy *et al.* [79,80] have systematically randomly varied many binary evolution parameters simultaneously, comparing them against an observed sample (of binary pulsars). While this previous study also used a Bayesian, single-event-likelihood-based approach to assess the likelihood of given population models, our investigation is the first to carefully interpolate between choices of formation parameters (see, however, the thesis work of Delfavero [81]). The content in this section is based on this prior work, whose pertinent results we summarize for self-completeness.

1. StarTrack simulations

Synthetic universes are generated from a sequence of distinct StarTrack runs, applied to a fixed number of isolated binaries all born at a fixed reference time. For each set of binary evolution parameters, StarTrack is applied to a range of progenitor metallicities. With each run, StarTrack evolves pairs of stars, accounting for accretion, tidal interactions, stellar wind, metallicity, gravitational radiation, magnetic braking, compact object recoil kicks, pair-production instability, and many more physical processes. It uses phenomenological models for supernovae to determine the properties of remnant black holes and neutron stars [69,82]. Among its many outputs are the expected population of compact binaries—BBH, BNS, and NSBH systems—characterized as (weighted) samples from the distribution of merging binaries.

The initial population of stars in a StarTrack simulation is drawn from a Kroupa initial mass function (IMF) [83–85],

$$\Psi(m_1) \propto \left\{ \begin{array}{cc} m_1^{-1.3} & 0.08M_\odot \leq m_1 < 0.5M_\odot \\ m_1^{-2.2} & 0.5M_\odot \leq m_1 < 1.0M_\odot \\ m_1^{-\alpha_{\rm IMF}} & 1.0M_\odot < 150M_\odot \end{array} \right\}, \quad (1)$$

where we adopt $\alpha_{\rm IMF} = 2.35$ for the highest mass stars (consistent with [26,86]). The companion mass (m_2) is drawn uniformly in mass ratio (m_2/m_1) from $[q_{\rm min}, 1]$, where $q_{\rm min} = 0.08M_\odot/m_1$ represents the hydrogen burning limit for m_2 [87–89]. For computational efficiency, only binaries where $m_1 > 5M_\odot$ and $m_2 > 3M_\odot$ are evolved when simulating StarTrack populations of compact binaries, as only these systems can form black holes and neutron stars.

The first step in relating these StarTrack runs to a synthetic universe is describing them as the population of stars produced by a specific amount of star-forming mass. In other words, we compute the amount of star-forming gas $M_{\rm sim}$ that would be expected to produce the population of evolved binaries, accounting for the arbitrary thresholds used to improve computational efficiency. This is done by finding the mass efficiency $\lambda_{\rm sim}$ [90], where

$$\lambda = \frac{n}{N}\frac{f_{\rm cut}}{\langle M \rangle}, \quad (2)$$

where N is the number of total binaries simulated, n is the number of compact binary progenitors, $\langle M \rangle$ is the average mass of all binary progenitors, and $f_{\rm cut}$ accounts for the binaries that are cut to fit mass requirements.

$M_{\rm sim}$ must also account for systems that do not form binaries, systems which do not merge in the Hubble time, and a sea of low-mass stars. While the true fraction of stars that form binaries is unknown, the merger rate $[\rho(t|f_b)]$ per unit mass at time t for any choice of binary fraction f_b can be found in terms of the corresponding answer for $f_b = 1$ by using the following relationship [90]:

$$\rho(t|f_b) = \rho(t|f_b = 1)\frac{f_b(1 + \langle q \rangle)}{1 + f_b\langle q \rangle}, \quad (3)$$

where $\langle q \rangle = 0.5$ is the expected mass ratio (for uniform q; consistent with Sana *et al.* [91]), and $\rho(t|f_b = 1)$ is the merger rate versus cosmological time evaluated for $f_b = 1$. f_b is assumed to be $1/2$ unless otherwise noted.

One can find $M_{\rm sim}$, the mass representing a StarTrack simulated population, as

$$M_{\rm sim} = \frac{2f_b}{1 + f_b}\frac{n}{N}\frac{f_{\rm cut}}{\langle M \rangle}M_{\rm bin}, \quad (4)$$

where $M_{\rm bin}$ is the sum of the mass of all simulated binaries.

The output of StarTrack is a list of simulated compact binary mergers and their binary parameters $\vec{\lambda}$ for a single zero age main sequence (ZAMS) metallicity $\mathcal{Z}$ and a single

set of binary evolution model constraints (i.e., formation parameters) Λ. The binary parameters $\vec{\lambda}$ include m_1, m_2, and redshift at time of merger (z_m). Each simulation provides an estimate for how densely the simulation is populated in the space of $\vec{\lambda}$,

$$\rho_{\rm sim}(\vec{\lambda}) = \sum_i \delta(\vec{\lambda} - \vec{\lambda}_i), \tag{5}$$

where i indexes the coalescing binaries in that simulation. This expression is normalized as

$$N_{\rm sim} = \int_{\{\vec{\lambda}\}} \rho_{\rm sim}(\vec{\lambda}) {\rm d}\vec{\lambda}. \tag{6}$$

Though not used in this work, Eqs. (5) and (6) are conceptually helpful when connecting simulation Monte Carlo results to the explicit cosmological postprocessing performed below.

2. Single star and binary evolution assumptions

Beyond assuming an initial mass function and bookkeeping with regard to how sample mergers represent a simulation mass, there are many assumptions about individual and binary stars that deserve accounting. Exhaustively describing every assumption used by StarTrack is unnecessary, as StarTrack has been developed alongside literature [24,26,70]. However, in order to effectively compare assumptions made in this work to those of other groups currently studying binary evolution, we will review some of the most relevant assumptions.

Supernova engine.—The models M13–M19 are based on the recently studied M10 model [26] and differ in assumptions about kick velocity. For the models based on the M10 model, SN masses are drawn from the "rapid" SN engine of Fryer *et al.* [82], considering neutrino mass loss at compact object formation. For models based on M10, mass loss from neutrinos is 10%, regardless of source properties. These model strong effects from pulsational pair-instability supernova (PPISN) and strong pair-instability supernova (PISN), consistent with Belczynski *et al.* [76]. These models assume a 10% Bondi-Hoyle accretion rate onto NSBH during CE events. Remnant black hole spins for models based on M10 are computed using Geneva stellar evolution models, following [26].

The K series of models (K0100–K0598) are derived from the M30 model [26] rather than M10. While the M30 model incorporated a rapid SN engine with weak PISN/PPISN effects [76,82], K0100-K0598 incorporate a "delayed" SN engine (see the same papers). Mass loss from neutrinos in these models is divided based on source properties. In massive black holes ($>3M_\odot$), 10% of the SN remnant mass is lost to neutrino emission, while 1% loss is assumed for less massive remnants. These models assume a 5% Bondi-Hoyle accretion rate onto NSBH during CE events. Remnant black hole spins for models based on M30 are based on MESA simulations [26].

All models assume a maximum neutron star mass of $2.5M_\odot$. Rather than assuming a fixed BBH efficiency, systems are evolved and the end of their evolution is determined by the properties of each system.

Supernova recoil kicks and fallback.—We note that, while the M10 model does have a reduction in kick velocity due to matter falling back onto a new compact remnant, M13–M19 do not. Unless otherwise noted, SN recoil kick velocities for new compact remnants are drawn from a single-peaked Maxwellian distribution characterized by the dispersion $\sigma_{\rm eff}$ (with units km/s). This velocity is not reduced by fallback.

A one-parameter family of models varying this dispersion (between 10 and 265 km/s) has been previously presented [70,76] and compared to GW observations in [54]. These models are denoted M13, M14, M15, M16, M17, and M18 (as well as M19, which was generated for this publication). This parameter is also varied in our higher-dimensional studies.

The K series models based on M30 presented in this publication are described by the same kick model as M13–M19.

Other, more complex SN recoil kick models exist and have been studied in other work [26,47,82,92–96]. It is important to keep in mind the uncertainty introduced by this simplified kick model when interpreting our results. For a discussion of the mechanisms involved with both fallback-reduced kicks and non-fallback-reduced kicks, see Sec. 6.2 of [25].

Mass transfer.—Roche-lobe overflow is the transfer of mass from one star (the donor) to its companion (the accretor) when the atmosphere of the donor expands beyond the region where mass is gravitationally bound to just that star. This transfer occurs near the point between two stars where their gravitational pull cancels out. Roche-lobe overflow can be stable or unstable (e.g., if the donor's Roche lobe shrinks faster than its volume during mass transfer). Instabilities can lead to a merger or common-envelope phase. Stable Roche-lobe overflow can be conservative or nonconservative. For (dynamically) stable nonconservative Roche-lobe overflow, we adopt the formalism seen in Rappaport *et al.* [97,98] and later [62].

The fraction of mass lost by the donor which is accreted onto its companion is f_a. Therefore, $1 - f_a$ is the amount of matter which becomes unbound and is lost by the system. Some angular momentum is lost by this ejected material, described by the equation

$$\delta J = \beta \delta \dot{M}_1 (1 - f_a) \frac{2\pi a^2}{P}, \tag{7}$$

where $\delta \dot{M}_1$ is an infinitesimal amount of mass lost by the donor, δJ is a small amount of angular momentum carried

by matter ejected from the system, P is the orbital period, and a is the semimajor axis of the orbit. This angular momentum loss to ejected material is constrained by an efficiency (β), which is also referred to as the specific angular momentum of the ejected material.

In our one-dimensional study, these parameters are fixed ($f_a = 0.5$ and $\beta = 1.0$). In our higher-dimensional study, we vary these parameters in order to demonstrate the effectiveness of observation-driven constraints on these parameters from gravitational-wave events.

For unstable Roche-lobe overflow resulting in a common envelope, we adopt methodology consistent with [26] for common-envelope evolution. In the models presented by this work, common-envelope efficiency (as often described by $\alpha_{\rm CE}$) is set equal to unity. Some work has been done to study $\alpha_{\rm CE}$ (e.g., [99,100]), however, there is still much that is not understood about common-envelope evolution. The common-envelope binding energy (as often described by $\lambda_{\rm CE}$) is consistent with [26], which is adapted from [101–103].

Stellar wind.—Consistent with other literature on StarTrack [26,69], we start from standard Vink wind models [104]. However, inhomogeneities and clumping for line-driven winds from galactic [105–107] and Small Magellanic Cloud [108–111] sources have shown that Vink winds may overestimate mass-loss rates in massive stars. Theoretical and observational studies of this "weak wind phenomenon" [109,112–117] suggest that mass-loss rates may be overestimated by a factor of about 3.

For models discussed in Sec. IV, we implement a scaling reduction in stellar wind mass-loss rates compared to the standard Vink model [104]. For a factor of 3 reduction, this scale factor ($f_{\rm wind1}$ for hydrogen-dominated stars) would have a value of $1/3$. For helium-dominated stars, we leave this scale factor "off" ($f_{\rm wind2} = 1.0$). This reduction in mass-loss rates due to stellar wind was introduced to StarTrack by Belczynski *et al.* [78]. One of the major goals of this work is to test how these lower winds impact properties of the merger population.

3. Cosmological postprocessing

The StarTrack team has developed routines to generate synthetic universes from an underlying set of StarTrack simulations [26,68,75]. These postprocessing routines draw samples from the StarTrack simulations, assigning each simulated binary weight that represents the expected merger rate in each simulated universe. This method of drawing from multiple simulations at different ZAMS metallicities yields a distribution that can be compared to a particular epoch of star formation in the history of the Universe.

In this work, we follow the procedures described in Sec. 2.6 of [26] in order to describe our choices of star formation rate density (SFRD), galaxy stellar mass function (GSMF), and mass-metallicity relation (MZR). We note that these choices can have a dramatic impact on the predicted rates of compact binary mergers (as explored by [20]). Future work may look further to explore these choices. Specifically, we adopt the Madau and Fragos [118] SFRD, with an IMF-dependent correction factor; see Eq. (1) of [118].

Also following from Madau and Fragos [118] (and, subsequently, [26,68], we adopt a MZR so the average metallicity versus redshift satisfies Eq. (6) of [118] (which is inspired by [119]),

$$\log Z/Z_\odot = 0.153 - 0.074 z^{1.34}. \tag{8}$$

This mass-metallicity relation is enforced by dividing the history of the Universe into $\Delta t = 10^8$ yr epochs, and inferring a mass distribution informed by redshift. Each epoch of evolutionary history is characterized by a distribution of galaxy masses (GSMF). We adopt a Schechter-type [120] GSMF from [121], frozen beyond redshift $z = 4$ (consistent with [68]).

Rather than assigning every galaxy in a given epoch the same metallicity, galaxy samples are assigned a metallicity by assuming a Gaussian where the mean metallicity ($\bar{\mathcal{Z}}$) at a given redshift is assumed from Eq. (8) and $\sigma\mathcal{Z} = \exp(-0.5)\bar{\mathcal{Z}}$ (i.e., 0.5 dex). The percent point function (inverse of the cumulative distribution function) of the Gaussian is sampled uniformly in a space truncated on either side by 11 standard deviations.

We adopt a solar metallicity as $Z_\odot = 0.02$. As there is not a StarTrack simulation for every possible metallicity value, these galaxies are gathered into metallicity "bins" representing the closest metallicity value for which there is a StarTrack simulation. The metallicity bins included in our study are as follows: $\mathcal{Z} \in \{0.0001, 0.0002, 0.0003, 0.0004, 0.0005, 0.0006, 0.0007, 0.0008, 0.0009, 0.001, 0.0015, 0.002, 0.0025, 0.003, 0.0035, 0.004, 0.0045, 0.005, 0.0055, 0.006, 0.0065, 0.007, 0.0075, 0.008, 0.0085, 0009, 0.0095, 0.01, 0.015, 0.02, 0.025, 0.03\}$ [26]. Figure 1 depicts this sampling, from the Madau and Fragos models [118].

Although each metallicity bin requires a separate StarTrack simulation, each time bin does not, as it is only used to construct a distribution in the ZAMS metallicity of sources at a given time in the history of the Universe. The weight function that we need to predict compact binary formation is now simply

$$\rho_{\Lambda,\mathcal{Z},\Delta t}(\vec{\lambda}) = \frac{M_{\Lambda,\mathcal{Z},\Delta t}}{M_{\Lambda,\{\mathcal{Z}\},\Delta t}} \frac{\mathrm{SFR}(z)}{M_{\rm sim}}, \tag{9}$$

where $\mathrm{SFR}(t)$ is the cosmological star formation rate, for time bins that ultimately correspond to a redshift. Here, $M_{\Lambda,\mathcal{Z},\Delta t}$ is the mass attributed to a StarTrack simulation with formation parameters Λ and metallicity $\mathcal{Z}$ for a particular epoch of time Δt. Additionally, $M_{\Lambda,\{\mathcal{Z}\},\Delta t}$ is the mass

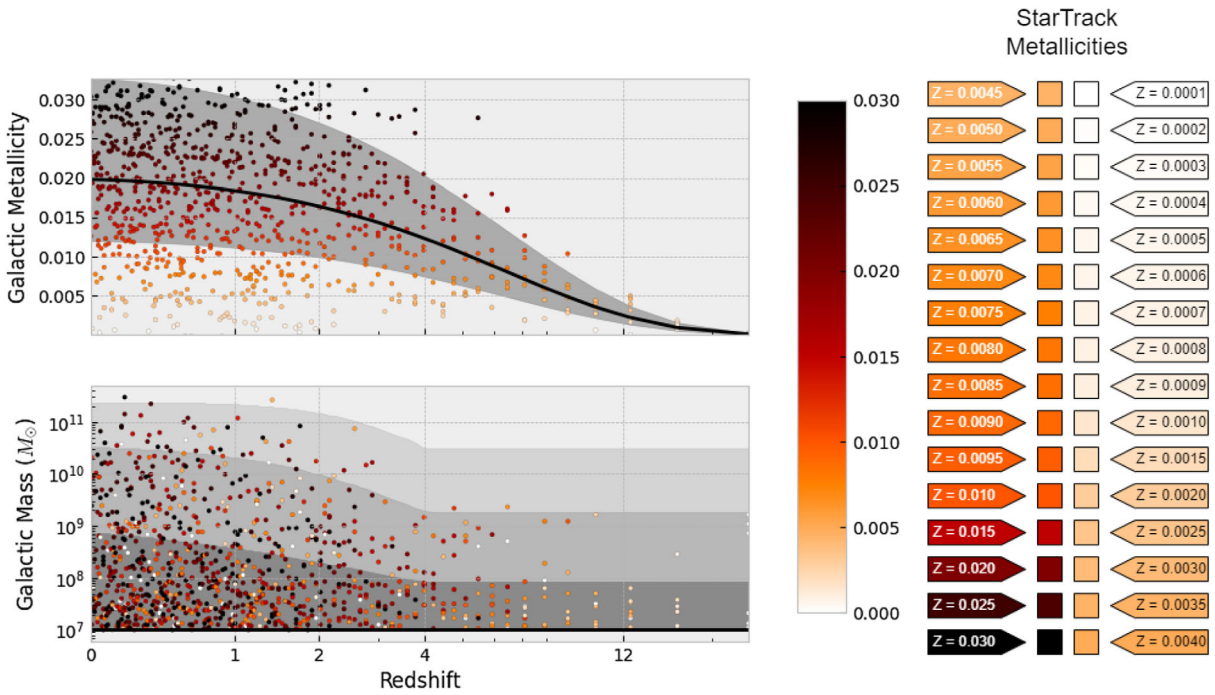

FIG. 1. Metallicity and mass distributions of star-forming material as a function of cosmological redshift: During postprocessing, star formation in each epoch of the Universe's history is represented by sampling galactic metallicity and star-forming mass distributions, assigning each galaxy to the nearest StarTrack metallicity bin and scaling StarTrack simulation masses by the mass of each galaxy. This enables a physically motivated accounting of star formation in each epoch of the Universe's history. Top left: the Madau and Fragos [118] metallicity dependence on redshift assumed in this work, where the black line follows Eq. (6) of [118]. Samples (colored by metallicity) are drawn from the cumulative distribution function (CDF) of the one-dimensional Gaussian with an assumed uncertainty of 0.5 dex (gray shaded region), consistent with prior work [26]. Bottom left: the Madau and Fragos [118] galactic star-forming mass dependence on redshift [see Eq. (1) of [118]). Shaded regions represent the 68%, 95%, and 99.7% confidence regions. Samples are again colored by metallicity. Right: the StarTrack metallicity bins used in this study. Each sample is assigned to a bin most closely associated with its given metallicity.

attributed to a particular epoch of time Δt for a particular StarTrack simulation with parameters Λ.

These weights are assigned to mergers in the output of StarTrack for each metallicity bin, and the sample population is now weighted correctly to represent the physical universe. Following this, the merger density for a synthetic universe is

$$\rho_\Lambda(\vec{\lambda}) = \sum_{\Delta t, \mathcal{Z}} \rho_{\Lambda,\mathcal{Z},\Delta t}(\vec{\lambda}) \Delta t \Delta \mathcal{Z}. \tag{10}$$

Throughout the rest of this paper, $\rho_\Lambda(\vec{\lambda})$ refers to the merger rate density for a synthetic universe constrained by the formation parameters Λ (with units of $\mathrm{Mpc}^{-3}\,\mathrm{yr}^{-1}[\vec{\lambda}]^{-1}$). This density is ultimately composed of the discrete merger samples

$$\rho(\vec{\lambda}) = \sum_i s_i \delta(\vec{\lambda} - \vec{\lambda}_i), \tag{11}$$

where s_i is the weight given to a particular sample merger.

B. Relating detected and observed populations

Our single-detector model for network sensitivity relates the populations of compact binary mergers assembled by our simulations to the observed population of gravitational-wave events. In order to perform that calculation, we make use of the merger samples and their weights to perform an integral over the sample population. The work in this section follows [75].

The expected gravitational-wave detection rate for a sample of the merger population from a given synthetic universe, characterized by formation parameters Λ [compare to Eq. (5) of [75]], is given by

$$R_\Lambda(\vec{\lambda}) = \rho(\vec{\lambda}) p_{\mathrm{det}}(\vec{\lambda}) \frac{\mathrm{d}V_c}{\mathrm{d}z_m} \frac{\mathrm{d}t_m}{\mathrm{d}t_{\mathrm{det}}}. \tag{12}$$

Here, $\frac{\mathrm{d}t_m}{\mathrm{d}t_{\mathrm{det}}} = \frac{1}{1+z}$ is the factor relating merger time and detector time. p_{det} is the detection probability [see Eq. (15)]. Equation (6) of [75] describes the differential comoving volume,

$$\frac{\mathrm{d}V_c}{\mathrm{d}z} = \frac{4\pi c}{H_0}\frac{D_c^2(z)}{E(z)}, \tag{13}$$

with comoving distance $D(z)$ and the dimensionless cosmological scale factor $E(z)$ [75]. In our calculations, we use the conventional Planck 2015 cosmology [122], implemented through Astropy for cosmological quantities such as $\mathrm{d}V_c/\mathrm{d}z$ [123,124].

The total number of gravitational-wave detections of a given kind ($\alpha \in \{\mathrm{BBH}, \mathrm{BNS}, \mathrm{NSBH}\}$) expected of a simulated universe is given by

$$\mu_{\Lambda,\alpha} = T_{\mathrm{obs}} \iiint_0^\infty R_{\Lambda,\alpha}(m_1, m_2, z_m)\mathrm{d}m_1\mathrm{d}m_2\mathrm{d}z_m, \tag{14}$$

where other merger parameters $\vec{\lambda}$ have been marginalized out. T_{obs} is the observing time for a run of the gravitational-wave observatories (LIGO and/or Virgo). Finally, types of mergers α are distinguished by a simple mass threshold ($m > 2.5 \rightarrow$ BH; $m < 2.5 \rightarrow$ NS).

Performing this integral over all the sample mergers for a StarTrack synthetic universe with one set of model assumptions (the formation parameters Λ) yields an expected number of gravitational-wave observations from ground-based observatories with those assumptions. The density of these predicted detection rates for each synthetic universe can also be interpreted in one- and two-dimensional marginalizations, providing an insightful glimpse into the predicted population of compact binaries in a synthetic universe (see Fig. 2). By comparing these predicted detection rates and populations to observations, we will limit the range of formation parameters motivated by Bayesian inference, described in greater detail in Sec. II C.

1. Detection probability

For interferometers like LIGO and Virgo, the detection probability depends strongly on the properties of each source. The process of detection is a complex process, depending on search pipelines and data quality vetoes that involve many human choices [10,63,126–128]. We cannot hope to reproduce this full process across the many potential observing runs each of our simulations can produce. We make a standard assumption that our survey can be approximated by a single interferometer, with a detection being defined as producing a signal-to-noise ratio (SNR) greater than a threshold, which we choose as $\rho_{\mathrm{thr}} = 8$. Using this approximation and averaging over all source orientations, the detection probability for a source with specific intrinsic parameters and redshift ($\vec{\lambda}$) but averaged over the sky and all source orientations can be expressed as a detection *probability* $p_{\mathrm{det}}(\vec{\lambda})$. When evaluating this expression, we need the SNR for an optimally located and oriented binary with parameters $\vec{\lambda}$, which in turn depends on our assumptions about our fiducial detector's sensitivity.

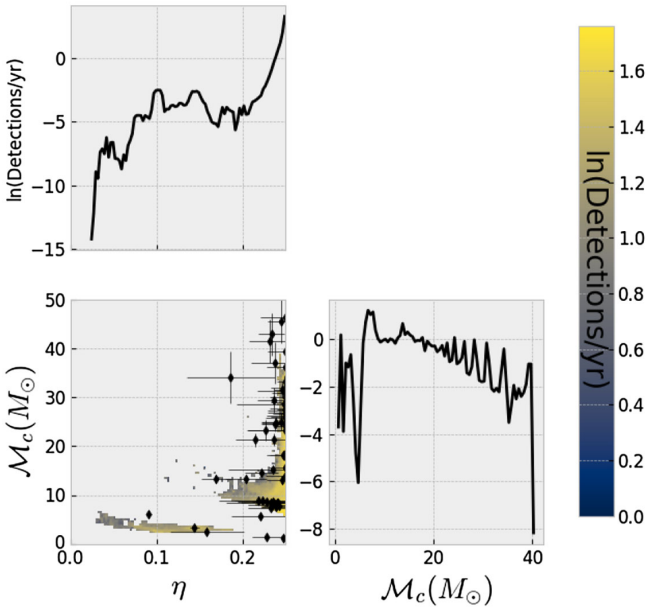

FIG. 2. Off-diagonal: a two-dimensional histogram illustrates an example of the predicted mass distribution of detections [$\mathcal{R}_d et(\mathcal{M}_c, \eta)$—reparametrized from m_1 and m_2; see Eq. (12)] for the M15 model (see Secs. II A 2 and III for more about M15). Also plotted are maximum likelihood estimate (MLE) parameter values (see Fig. 5 of [125]) for the confident GW events discussed by the LIGO/Virgo/KAGRA Collaborations in their rates and populations study following the third observing run of the ground-based gravitational-wave observatories [3]. Diagonal: one-dimensional detection-weighted densities for predicted detections in M15 in $\mathcal{M}_c$ and η. Notice the distinct lack of predicted events in the lower mass gap and of high-mass events in the $40 - 50M_\odot$ range.

From the second observing run (O2) catalog, we see that the BNS range for the LIGO Hanford Observatory (LHO) and LIGO Livingston Observatory (LLO) was up to 80 Mpc [63]. As in previous work, this corresponds to a high sensitivity point spread distribution (PSD) for early LIGO observation runs (the "SimNoisePSDaLIGOEarlyHighSensitivityP1200087" PSD included in LALSuite) [129,130]. For the first/second part of O3, we see that the BNS range for LHO is 135/133 Mpc and 108/115 Mpc for LLO [64,66]. The sensitivity of Virgo is not considered in our single-detector model. For O3, we use an optimistic model with the "SimNoisePSDaLIGOaLIGO140MpcT1800545" PSD included in LALSuite; this allows us to include a correction factor to account for the time-volume estimate for O3 [3,129–131].

In our work, the SNR is calculated for each simulated binary in every synthetic universe (trained using the LALSuite optimal matched-filter SNR for each PSD mentioned above; see Appendix A) [130,132]. We also define a threshold SNR, $\mathrm{SNR}_{\mathrm{thr}} = 8$, above which the detection is

counted. Following Dominik *et al.* [75], we find the probability of detection,

$$p_{\rm det}(\lambda) = P\left(\frac{\rm SNR_{thr}}{\rm SNR(\lambda)}\right), \tag{15}$$

where $\mathrm{P}(w)$ is interpolated from results tabulated by other groups [133].

C. Bayesian inference for populations

In the previous sections, we discussed our methods for using StarTrack simulations to predict compact binary merger rates for a simulated universe and calculating predicted gravitational-wave detection rates associated with those merger densities. Now, we set about using those tools to draw conclusions about the Universe, expanding on the Bayesian framework described by [4,54,75,81].

The predicted gravitational-wave detections $\{d_j\}$ and merger population $\rho_{\Lambda,\alpha}$ can be compared with a set of observations ($\{d_j\}$) using an inhomogeneous Poisson point process [1,53–56]. The likelihood associated with this process can be broken down,

$$\mathrm{P}(\{d_j\}|\Lambda) = \mathrm{P}(\mu|\Lambda)\prod_j \mathrm{P}(d_j|\Lambda), \tag{16}$$

where μ is the number of *observed* GW detections and $\mathrm{P}(\{d_j\}|\Lambda)$ is ultimately the quantity used to evaluate the agreement between observations and the predicted detection rates and merger populations for a simulation ($\mu_{\Lambda,\alpha}$ and ρ_Λ, for kind $\alpha \in \{\mathrm{BBH}, \mathrm{BNS}, \mathrm{NSBH}\}$). Throughout this work, we refer to $\mathrm{P}(\{d_j\}|\Lambda)$ as the "joint likelihood," $\mathrm{P}(\mu|\Lambda)$ as the "rate likelihood," and $\prod_j \mathrm{P}(d_j|\Lambda)$ as the "shape likelihood."

1. Rate likelihood

The rate likelihood is calculated the same as a standard Poisson point process for each type of event,

$$\mathrm{P}(\mu_\alpha|\Lambda) = e^{-\mu_{\Lambda,\alpha}}\frac{\mu_\Lambda^{N_\alpha}}{N_\alpha!}, \tag{17}$$

where N_α is the number of observed GW sources of a given type. The total rate likelihood is the product of these,

$$\mathrm{P}(\mu|\Lambda) = \mathrm{P}(\mu_{\rm BBH}|\Lambda)\mathrm{P}(\mu_{\rm BNS}|\Lambda)\mathrm{P}(\mu_{\rm NSBH}|\Lambda). \tag{18}$$

For a breakdown of how to efficiently calculate this quantity directly in the log space, see Sec. 4.1.1 of [81].

2. Shape and joint likelihood

The shape likelihood of a synthetic universe with formation parameters Λ describes the probability that each individual GW source could be produced in a universe where those assumptions are true. More specifically, it measures the agreement of the samples described by $\rho_\Lambda(\vec{\lambda})$ to the shape of the likelihood function for the binary parameters of each detection $\mathcal{L}_j(\vec{\lambda})$. This likelihood is marginalized over the merger samples,

$$\begin{aligned}\mathrm{P}(d_j|\Lambda) &= \int_{\{\vec{\lambda}\}} \mathrm{P}(d_j|\vec{\lambda},\Lambda)\mathrm{P}(\vec{\lambda}|\Lambda)\mathrm{d}\vec{\lambda} \\ &= \int_{\{\vec{\lambda}\}} \bar{\rho}_\Lambda(\vec{\lambda})\mathcal{L}_j(\vec{\lambda})\mathrm{d}\vec{\lambda},\end{aligned} \tag{19}$$

where $\bar{\rho}_\Lambda(\vec{\lambda}) = \rho_\Lambda(\vec{\lambda})/\int_{\{\vec{\lambda}\}}\rho_\Lambda(\vec{\lambda}')\mathrm{d}\vec{\lambda}'$.

This marginalization is carried out over the entire population of 10^8 sample mergers in a synthetic universe, for each GW observation from a given observing run. We make use of bounded (truncated) multivariate normal distributions to calculate this likelihood, described in separate publications [81,125,134]. While the estimated likelihood for individual gravitational-wave events can have more complex morphology, these bounded multivariate normal distributions have been demonstrated to lose less information than waveform systematics [125]. As relativistic waveforms are most sensitive to chirp mass and symmetric mass ratio and Gaussian noise is expected in these coordinates, these coordinates (in the source frame of reference) are used for evaluating this likelihood. Putting this together with our rate likelihood, the joint likelihood can be expressed [equivalent to Eq. (4) of [4]],

$$\mathrm{P}(\{d_j\}|\Lambda) = K_{\rm rate}e^{-\mu_\Lambda}\prod_j\left[\int_{\{\vec{\lambda}\}}\mathcal{L}_j(\vec{\lambda})\bar{\rho}_\Lambda(\vec{\lambda})\mathrm{d}\vec{\lambda}\right], \tag{20}$$

where

$$K_{\rm rate} = \frac{\mu_\Lambda^{N_{\rm BBH}}}{N_{\rm BBH}!}\frac{\mu_\Lambda^{N_{\rm BNS}}}{N_{\rm BNS}!}\frac{\mu_\Lambda^{N_{\rm NSBH}}}{N_{\rm NSBH}!}. \tag{21}$$

3. Model interpolation and posterior generation

Interpolating each type of detection rate and likelihood in the formation parameter space is valuable in one- and higher-dimensional studies (see Figs. 3 and 9, respectively). We use Gaussian process regression to implement such interpolations and briefly summarize this method: For brevity and to be consistent with conventional notation, we denote $\vec{\lambda}$ by x and the quantity being fit by y. In this approach, we estimate the expected value of $y(x)$ from data x_* and values y_* via

$$\langle y(x)\rangle = \sum_{\gamma,\gamma'} k(x, x_{*,\gamma})(K^{-1})_{\gamma,\gamma'}y_{*,\gamma'}, \tag{22}$$

where γ is an integer running over the number of training samples in (x_*, y_*) and where the matrix $K = k(x_\gamma, x_{\gamma'})y_*$. The expected variance at x is given by $K(x,x)^{-1}$. We employ a kernel function $k(x,x')$, which allows for uncertainty in each estimated training point's value $y_{*,\gamma}$, reflecting systematic uncertainty in the input values. We use a conventional piecewise-polynomial kernel to ensure compact support [135]; the implementation of this kernel is discussed in the context of SNR in Appendix A.

One advantage of a Gaussian process is that it can accept information about uncertainties in training data. To account for systematic uncertainties in our binary evolution inputs, we adopt a fiducial (and optimistic) systematic uncertainty of 10% in the event rate and thus 0.1μ in the log-likelihood. We emphasize that our specific choice is an arbitrary division between nominally subdominant and dominant parameters (i.e., we assert parameters with less than 10% effect are ignorable and account for them with systematic error). Neither the specific nominal systematic error nor our limited model space are intended as definitive or even representative exploration of all possible parameters and uncertainties; rather, these choices allow us to illustrate the method of this paper with realistic models and assumptions, while allowing us to defer the exhaustive exploration of many more parameters to future work. When plotting our interpolated quantities, we show the nominal 1σ uncertainty predicted by the Gaussian process.

We use two different methods for interpolating the joint likelihood: (1) direct interpolation of $\mathrm{P}(\{d_j\}|\Lambda)$ for each simulation and (2) interpolation of $\mu_\alpha(\Lambda)$ for each type of merger and interpolation of $\sum_j \mathrm{P}(d_j|\Lambda)$ (i.e., the shape likelihood). By interpolating these quantities, we can construct the joint likelihood with Eq. (16) for each sample.

Of these, the first is more direct, and the second is more useful in a sparsely sampled space.

Though sampling from a bounded multivariate normal distribution (i.e., truncated Gaussian) is used to propose new simulations for the models in Sec. IV, an interpolated model can be used for sampling when there is not a simple peak. When sampling from an interpolated rate, shape, or joint likelihood to construct a posterior for that quantity, we sample uniformly in the formation parameter space and find a weight for each point from the Gaussian process (assuming a uniform prior in Λ).

4. Inputs from GW observations

The third observation run of the LIGO/Virgo gravitational-wave observatories have increased the number of GW observations to around 90 [66]. These new observations extend to significantly higher mass [136,137], within the lower mass gap [15], more extreme mass ratios [14,15], and multiple NSBH events [13,64–66]. These objects' existence strongly constrain formation models. For example, the surprising secondary mass of GW190814 [15] may constrain models for SN, as not all such models can produce events in the lower mass gap [16]. As we show below, a joint analysis of the whole population provides very stringent model constraints, which are difficult to satisfy without allowing for the possibility of substantial systematic error.

In the analysis below, we use Gaussian approximations to the likelihood of the confident events (excluding GW190521) from the third observing run of LIGO/Virgo [3], as a function of mass alone. GW190521 in particular is excluded as it would require nonstandard physical assumptions to be formed in isolated binary evolution [138] that we do not test in this current study. Alternatively, it may have formed through dynamical interactions in a dense stellar cluster [34,35]. In our preliminary analysis, we marginalize over and do not attempt to reproduce binary spin. The specific parameters of these single-event likelihoods are described in [125].

III. ONE-DIMENSIONAL STUDY: NATAL KICK VELOCITY

To illustrate our methods, we first use a simple low-dimensional approach that employs a series of StarTrack models in which we alter only one evolutionary parameter: the dispersion parameter of the NS/BH SN recoil kick velocity (σ_{eff}). This parameter has been thoroughly explored in previous work, notably in Wysocki *et al.* [54]. We emphasize that in previous work with StarTrack, two types of models have been examined: models with fallback-suppressed SN recoil kicks, where the kick distribution depends on the amount of fallback, and homogeneous SN recoil kicks, where the same distribution is applied to all compact objects, independent of fallback. In this work, we explore the latter.

As we show below, we find that for these models the merger rate varies strongly and the mass distribution weakly versus SN recoil kick strength. The merger rate is highly informative and the mass distribution weakly informative about SN recoil kicks.

For these models, as the SN recoil kick velocity increases, an increasing fraction of compact binaries are disrupted, causing the compact object merger and detection rate *overall* to vary strongly with kick strength. For example, Fig. 3 shows the predicted detections for an observing run as a function of SN recoil kick strength, compared to the first part of LIGO's third observing run (O3a) [64,65]. Given the other assumptions in our binary evolution simulations (refer to Sec. II A 2), the strength of fallback-independent SN recoil kicks would need to be large (between 70 and 200 km/s) to explain the overall number of observations in O3a.

By contrast, Fig. 4 shows the chirp mass distribution of observable gravitational-wave events for several choices of kick strength. Though the overall number varies substantially, the shape of the mass distribution changes relatively little, except for the relative proportions of BNS and NSBH

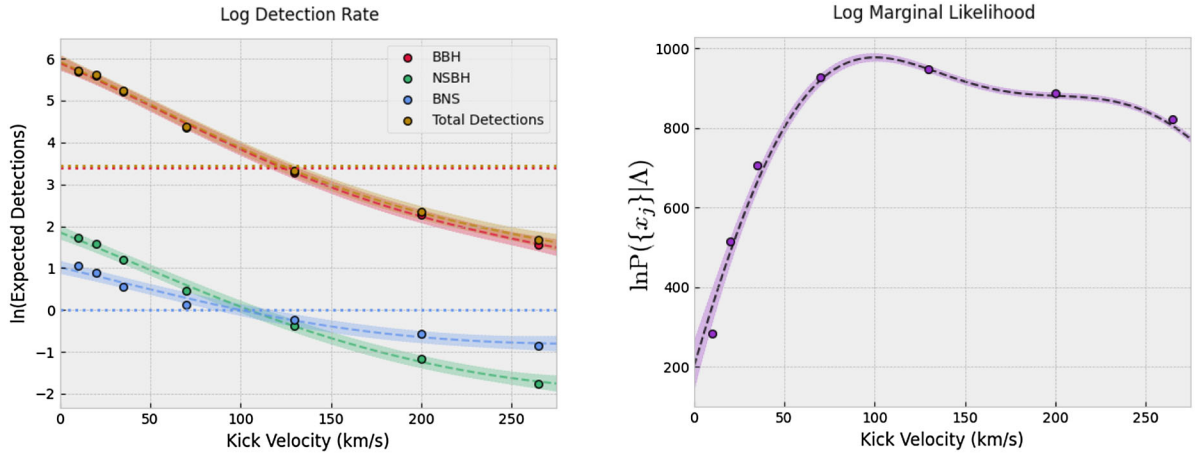

FIG. 3. Likelihood versus kick in O3a: Left: the log of the expected number of detections for models with a particular kick velocity. The scattered points are values calculated by StarTrack models. The dashed line is the mean prediction of the Gaussian process interpolator, where the shaded regions are regions of σ_{eff}. The horizontal dotted lines are the number of GW observations in O3a. Right: the joint likelihood distribution of the kick parameter, considering the merger rate as well as the distribution of observations in O3a. Again, the scattered points represent StarTrack models, the dashed line represents the mean prediction, and the region of σ_{eff} is shaded. The interpolation of the joint likelihood follows the second method outlined in Sec. II C 3, incorporating information from each type of event rate and the shape likelihood.

binaries (i.e., the shape of the chirp mass distribution at very low mass).

In this case, we gain relatively little additional information from comparing the observed masses to this limited model family (keeping in mind that the M13–M19 models do not include updated supernova physics such as the delayed timescale of shock propagation, which is necessary for the prediction of events in the lower mass gap such as GW190814 [15]; see Fig. 2). The mismatch between the shape of the observed population and the simulated population for this one-dimensional study (see Fig. 4), regardless of the chosen σ_{eff}, suggests that varying assumptions beyond just the dispersion of SN recoil kicks is necessary to develop our understanding of binary evolution. The higher-dimensional study better describes the properties of the observed detections.

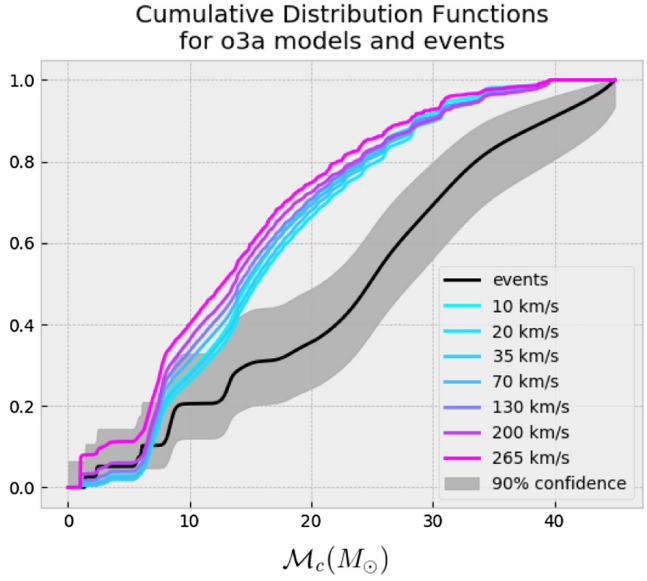

FIG. 4. Chirp mass cumulative distributions. One-dimensional SN recoil kick velocity survey. CDF in $\mathcal{M}_c$ for models M13–M19, for which σ_{eff} is varied. For comparison, a solid black line indicates the CDF for observations in the first part of LIGO/Virgo's third observing run (shaded gray region indicates 90% symmetric credible interval for those observations).

It follows that, in order to properly constrain the shape of the population, a higher-dimensional study has the capacity to further constrain these models in a way that this one-dimensional study does not.

Figure 3 shows the key result of this one-dimensional study: the marginal likelihood of each binary evolution model as a function of kick velocity. This likelihood incorporates not only information about the detection rate, but the properties of the observed gravitational-wave population (refer to Sec. II C for details about this calculation).

This likelihood can be used in a straightforward way to generate a posterior, by assuming a uniform prior in binary evolution parameters; we do not demonstrate this for the one-dimensional study, but provide examples in the four-dimensional study in the next section. As described above, our calculations favor substantial SN recoil kicks ($>$70 km/s) to explain the observed merger rates and masses. For O3 and this limited parameter survey, merger rates for all three event classes happen to be consistent with the same kick velocity: $\simeq$125 km/s (model M15; see Fig. 2 for the distribution of predicted detections for this model).

As discussed previously, systematic uncertainties (i.e., we only vary a subset of all binary evolution parameters,

TABLE I. Sampling methods for four-dimensional model space: Each row depicts the sampling method used for each subset of the four-dimensional parameter space models. With each subset of models, our inferred joint likelihood (natural log likelihood; lnL in this table) is better understood through iterative improvements. Truncated Gaussians rely on GWALK [125]. For all simulation parameters, see Appendix C.

Model IDs	Successful models	Sampling	Best ID	Best lnL
K0100-K0399	284	Uniform $f_a \in [0.1, 1.0]$, $\beta \in [0., 1.]$, $\sigma_{\rm eff} \in [0, 265]$, $f_{\rm wind1} \in [0.2, 1.0]$	K0358	55.468
K0400-K0499	97	Uniform $f_a \in [0.5, 1.0]$, $\beta \in [0., 1.]$, $\sigma_{\rm eff} \in [20., 150.]$, $f_{\rm wind1} \in [0.2, 1.0]$	K0483	62.001
K0500-K0519	20	Samples from truncated Gaussian fit to K0100-K0499	K0506	67.117
K0520-K0559	40	Samples from truncated Gaussian fit to K0100-K0519	K0559	67.995
K0560-K0563	4	Cherry picked	K0563	65.437

and the neglected parameters have a non-negligible effect) and uncertainties in our ability to correctly quantify GW survey systematics with our simple approximations propagate into uncertainties in our marginal likelihoods. We do note, however, that less information is lost due to our likelihood model than waveform systematics [125]. For simplicity, however, we generate posterior distributions for our binary evolution parameters (here, SN recoil kick $\sigma_{\rm eff}$) without propagating these systematic effects. (This choice also does not oversmooth incorrectly, inappropriate for the net correlated impact of some systematics like input SFR normalization, which influence all models with a common multiplicative factor.)

IV. FOUR-DIMENSIONAL STUDY

We now apply our method to the four-dimensional model family performed for this work. These 442 simulations cover three salient binary evolution parameters: $\sigma_{\rm eff}$, the dispersion parameter for the Maxwellian distribution from which SN recoil kick velocities are drawn (a single Maxwellian is used for BH and NS kicks, which are not reduced by fallback); f_a, a parameter characterizing the efficiency of mass transfer; and β, the specific angular momentum of the ejected material. Unlike the simulations described earlier, we also account for the suppression of mass loss due to stellar winds described by [78]; we vary the parameter $f_{\rm wind1}$ to account for this suppression in hydrogen-dominated stars, but keep $f_{\rm wind2} = 1$ fixed—indicating that mass loss is not suppressed for helium-dominated stars. Belczynski *et al.* [78] have demonstrated that a sufficient reduction ($f_{\rm wind1} \approx 0.2$) allows for the formation of much larger remnant objects from isolated binary evolution (such as GW190521). We begin with a uniform sampling in the space of these four formation parameters and iteratively refine a truncated Gaussian model to sample from regions of higher likelihood. Table I highlights that, though the space of formation parameters is first explored through samples drawn uniformly in the parameter space, at each iteration we were able to refine our model, and starting with the models labeled K0400 and higher, samples are drawn from a four-dimensional truncated Gaussian fit to the peak likelihood at hand-picked intervals (where points sampled from the Gaussian outside the bounds of the space of our formation parameters are disregarded). This allows us to iteratively refine the peak in joint likelihood.

Furthermore, for this family of models, we adopted a SN engine with delayed shock propagation, as needed to reproduce objects in the lower mass gap like the secondary in GW190814 [16,139]. We also consider the effect of weak pair-production instability in order to model pair-instability and pulsational pair-instability supernova; the latter of which expand the range of predicted high-mass remnant objects [26,76]. The simulations cover a broad range of possibilities, including models that are consistent with most of the confident detections reported in O3; Fig. 5 further illustrates this point [3].

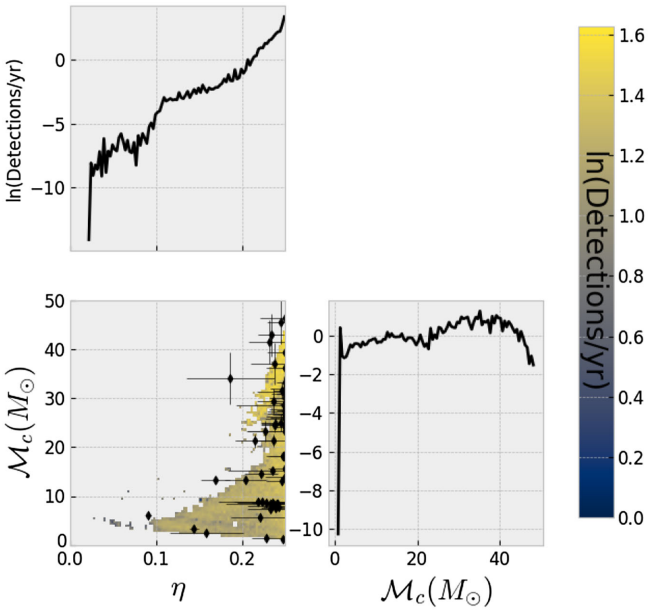

FIG. 5. Compare Fig. 2. Off-diagonal: a two-dimensional density of predicted detections for the K0559 model (in $\mathcal{M}_c$ and η). Also plotted are MLE parameter values for confident observations [3]. Diagonal: one-dimensional detection-weighted densities for K0559 in $\mathcal{M}_c$ and η. For this model, we note the absence of a distinct lower mass gap compared to the M15 model presented in Fig. 2 and an upper range of BBH chirp mass, which is well into the 40's of solar mass.

To highlight the diversity of these simulations, Fig. 8 shows the chirp mass distributions for our simulations. Similarly, Fig. 6 shows the expected number of BBH and BNS observations in O3, compared to current population models. Figure 7 catches a further glimpse into the dependence of the detection rate on each formation parameter and combination thereof.

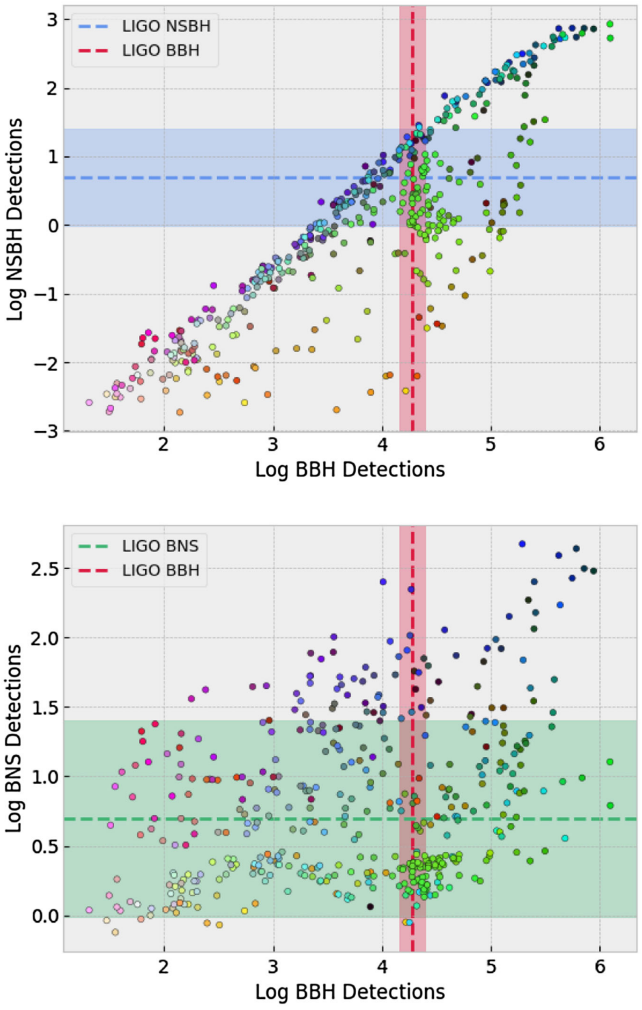

FIG. 6. Expected detection counts and empirical constraints. Scatter plot of the number of predicted BBH, NSBH, and BNS detections for the four-dimensional simulated model family examined in this work, in comparison with the observed number seen in the first three observing runs of ground-based gravitational-wave interferometers (consistent with [3]). Detection rates are expressed in natural logarithmic scale. Dashed lines indicate observations, with shaded regions indicating counting error $1/\sqrt{n_{\rm obs}}$; compare to [26]. The dots with dark borders denote results from our simulations. $\sigma_{\rm eff} \in [0, 265]$ km/s, $f_a \in [0.1, 1.0]$, and $f_{\rm wind1} \in [0.2, 1.0]$ encode the red, green, and blue pixel data ($\in [0, 1]$) for each model. This color map aids in identifying ranges of formation parameter values in the limited dimensions of this figure. The cluster of green samples largely correspond to simulations proposed using the truncated Gaussian model (see Table I).

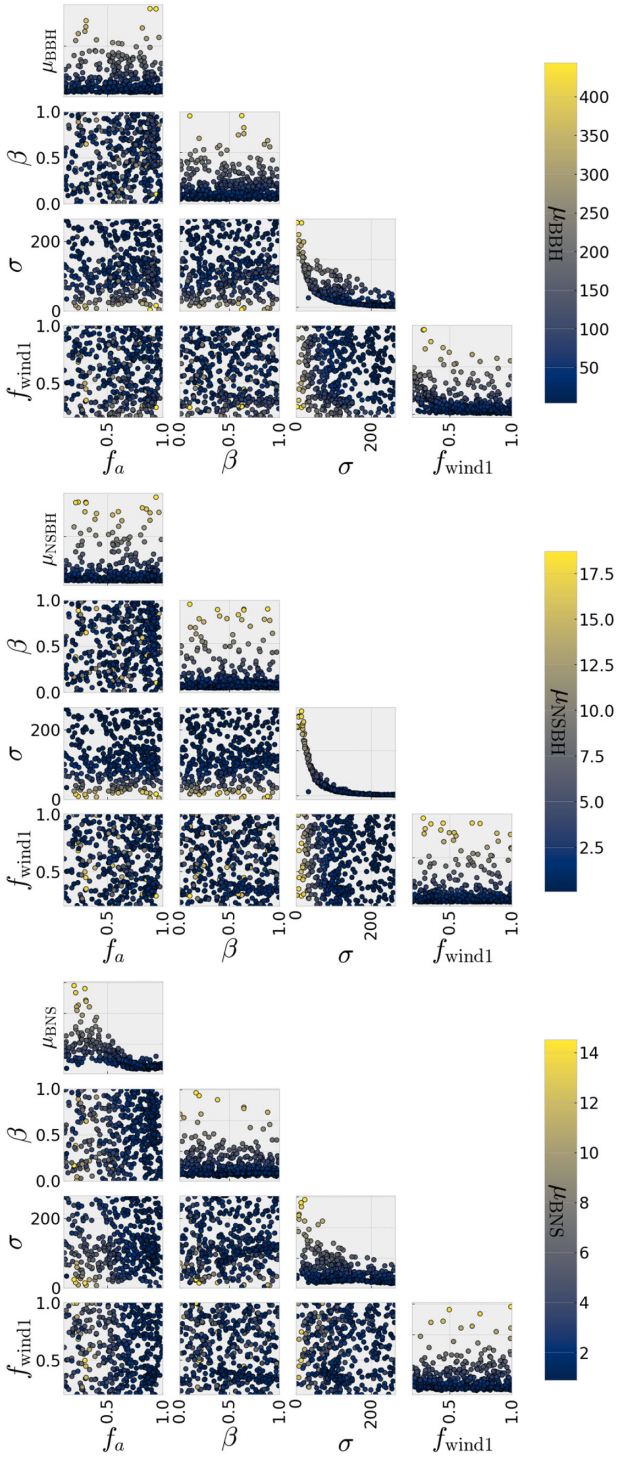

FIG. 7. Detection rates versus formation parameters: Scatter plot in formation parameter space of BBH (top), NSBH (center), and BNS (bottom) mergers, where the color scale indicates the detection rate for each simulation. Off-diagonal plots show a two-dimensional scatter in formation parameters (f_a, β, $\sigma_{\rm eff}$, and $f_{\rm wind1}$), while diagonal plots show a one-dimensional scatter (where the y axis is the detection rate; as also indicated by the color). Detection rates are estimated with the two-detector sensitivity and observing time from O3 [64,66].

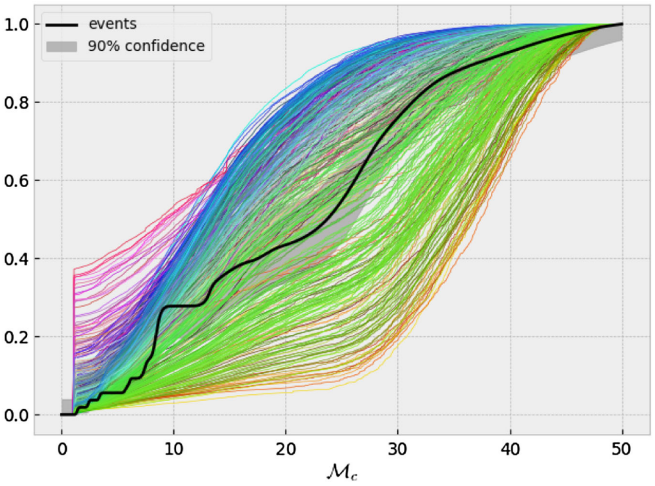

FIG. 8. Chirp mass cumulative distributions. Four-dimensional model survey. Chirp mass CDFs for the four-dimensional model family described in Sec. IV. The color scale encodes three model parameters as RGB values (RGB encode $\sigma_{\rm eff}$, f_a, $f_{\rm wind1}$, respectively). For comparison, the solid black line and gray region show the cumulative distribution function for O3 observations and the corresponding 90% credible interval, respectively.

Different formation parameters have strong impacts on different populations. For example, Fig. 7 shows how the detection rate changes versus the parameters in our study. For BBH, the merger rate is principally determined by $\sigma_{\rm eff}$, with a subdominant impact from $f_{\rm wind1}$ and other parameters. For BNS, the merger rate is determined by both f_a and $\sigma_{\rm eff}$. For NSBH, the merger rate is principally determined by $\sigma_{\rm eff}$, in a very tightly dependent manner.

Figure 7 also visually suggests what combinations of parameters are required to reproduce current event counts. For these models, a substantial $\sigma_{\rm eff}$ is required to predict the correct amount of BBH and NSBH detections. With only two reported observations so far, the BNS and NSBH merger rates are highly uncertain, and the observed counts are consistent with (but in modest tension with) what is expected for substantial SN recoil kicks.

Note that while the reported number of BBH observations seems very strongly constraining, systematic uncertainties highlighted in the previous section associated with subdominant parameters and input uncertainties imply that the absolute merger rate must be interpreted with caution. Similarly, even adopting the delayed SN engine and even not aggressively adjusting physics associated with the pair-instability gap, the reported chirp mass distribution can encompass most of the observations reported to date (see Fig. 8).

We can learn as much about our formation parameters from the shape of the mass distribution of predicted mergers as we can from the detection rates. We have evaluated the agreement of the masses of each sample detection from each simulation with each confident gravitational-wave observation from the first three observing

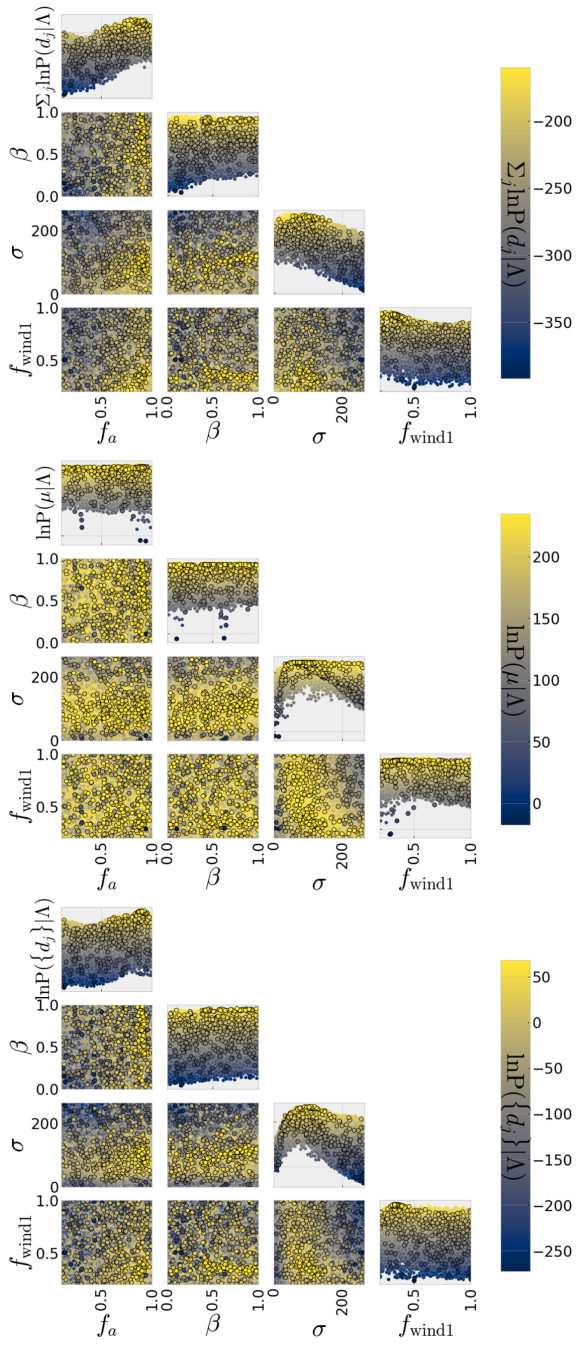

FIG. 9. Inferences on four-dimensional model constraints. Scatter plot in formation parameter space for quantities of interest (indicated by color): shape likelihood (top), rate likelihood (center), and joint likelihood (bottom). Off-diagonal plots show a two-dimensional scatter in formation parameters ($f_a, \beta, \sigma_{\rm eff}$, and $f_{\rm wind1}$), while diagonal plots show a one-dimensional scatter (where the y axis is the quantity of interest; as also indicated by the color). Larger dots with dark borders denote results from our full simulations; smaller background dots with white borders are posterior samples drawn from a uniform prior, weighted by interpolated likelihood. The scale indicated for the rate and shape likelihood can be used to asses their relative importance, as the joint likelihood is the sum (in natural log) of the two quantities. In contrast to Fig. 3, the joint likelihood is interpolated directly and sampled according to the method outlined in Sec. II C 3.

runs of ground-based detectors (consistent with [3]). This information about the shape of the distribution is described by the shape likelihood (see Sec. II C 2). The full inhomogeneous Poisson likelihood can be recomposed from the component rate and shape likelihood components, and we refer to this as the joint likelihood (see Sec. II C 2). Figure 9 displays the rate, shape, and joint likelihood to a constant (as a function of formation parameters). For these models, both the rate and shape likelihood carry a meaningful weight to the joint likelihood. This is especially noteworthy in the two-dimensional marginal likelihood between $\sigma_{\rm eff}$ and $f_{\rm wind1}$.

Figure 9 indicates that the shape of the distribution favors high accretion of mass lost by a donor during Roche-lobe mass transfer (f_a), as well as moderate specific angular momentum of ejected material (β). Furthermore, there is a preference for moderate SN recoil kicks. We also find that reduced mass-loss rates from stellar wind are substantially favored (indicated by a low $f_{\rm wind1}$), consistent with [26]. These trends are roughly followed by the joint likelihood as well.

For the most general likelihood distribution without a single clear peak, the interpolation of the rate, shape, and joint likelihood (as in Fig. 9) best characterizes what we have learned about our formation parameter assumptions by comparing simulations to observations. These interpolated likelihoods can then describe a posterior in those formation parameters in the region of highest likelihood. We do not claim to do this, as such an approach overstates our confidence in model systematics: we have only explored a small number of the many important parameters that impact binary evolution, and many omitted parameters and physics are well known to have a significant impact on observables.

This interpolated likelihood can then be sampled from, in order to propose new simulations and further grow our

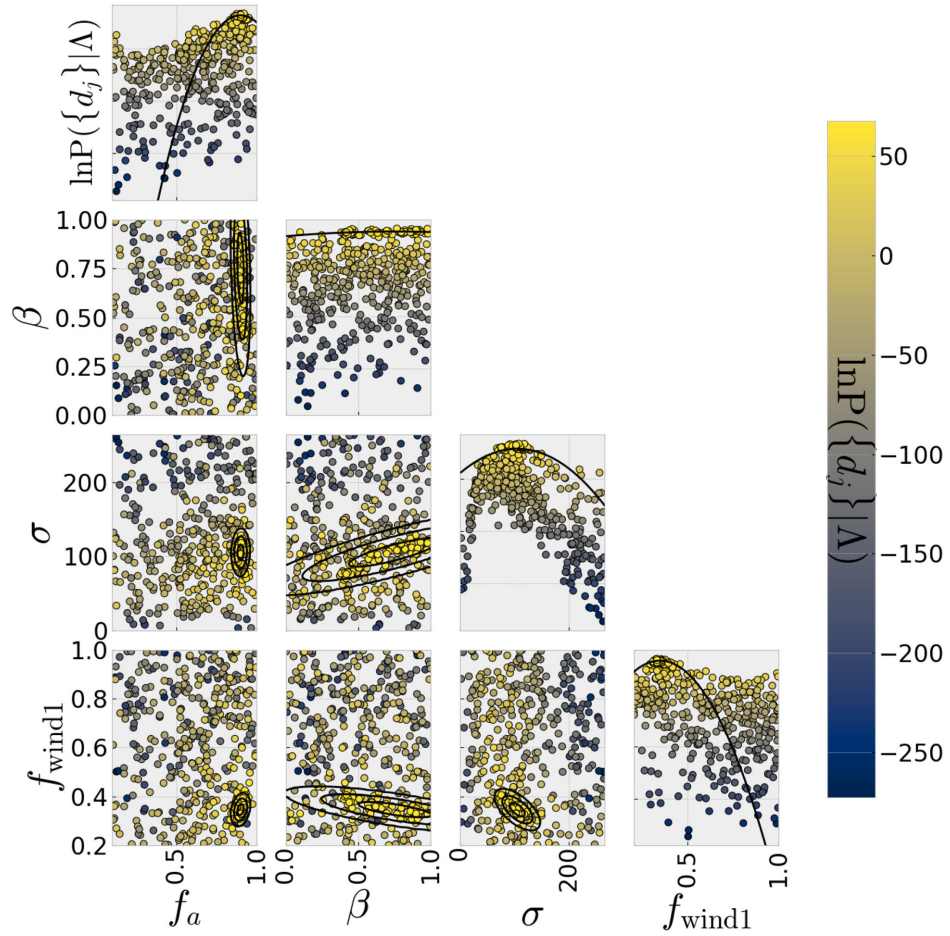

FIG. 10. Approximate Gaussian posterior large scatter points with dark borders represent each simulated universe (as in Fig. 9). A Gaussian approximation to the posterior has been drawn in black on one-dimensional diagonal plots; contours enclosing sampled regions of 1, 2, and 3 standard deviations are drawn on two-dimensional plots. Keep in mind that a Gaussian appears quadratic in the log space. This final approximation was fit to simulations within 7 of the maximum $\ln P(\{d_j\}|\Lambda)$ (27 simulations). Samples are drawn from Gaussians to propose the next batch of simulations, in a way that iteratively refines our ability to describe the relationships between parameters (see Table I). See also Appendix B for the properties of this Gaussian.

TABLE II. The parameters associated with the five best models, ranked by the inhomogeneous Poisson likelihood (see Sec. II C).

Model	f_a	β	$\sigma_{\rm eff}$	$f_{\rm wind1}$	$f_{\rm wind2}$	$\mu_{\rm BBH}$	$\mu_{\rm BNS}$	$\mu_{\rm NSBH}$	lnL_rate	lnL_shape	lnL_joint
K0559	0.922	0.768	108.299	0.328	1.000	95.015	1.453	1.218	231.346	−163.351	67.995
K0556	0.905	0.979	118.317	0.328	1.000	88.926	1.435	0.827	232.277	−164.747	67.529
K0506	0.898	0.459	92.364	0.353	1.000	92.756	1.317	1.557	231.964	−164.848	67.117
K0524	0.876	0.867	103.613	0.352	1.000	79.303	1.414	1.243	234.044	−167.049	66.995
K0542	0.907	0.594	101.609	0.376	1.000	72.266	1.369	1.365	234.436	−168.259	66.177

knowledge about the space of our assumed formation parameters. However, we have found that in this specific case there is a peak in likelihood that can be described locally by a Gaussian (see Fig. 10). This normal approximation allows us to characterize the best fitting parameters and their correlations. Fitting a bounded multivariate normal distribution to this likelihood greatly simplifies the process of sampling from it, and therefore we use this approximation to the likelihood in the region around this local maximum in order to propose new simulations. This sampling process only requires using known methods [140] of sampling from a multivariate normal distribution and discarding points sampled outside of the boundary (the limits of our formation parameter space) in order to propose new simulations.

In the future, this sampling may be done automatically by an algorithm. At present, each iteration requires choices about how sampling is accomplished. Table I describes this process for the K series of models presented here.

Through interpolating and/or modeling this joint likelihood and drawing samples from a likelihood model before launching subsequent simulations, we iteratively improve our understanding of the relationship between model parameters and likelihood in the four-dimensional space (see Table I). This method of hierarchical inference for constraining the isolated binary evolution formation channel for gravitational-wave populations is a benchmark for future studies of higher-dimensional population models.

Table II shows the parameters of the five most highly ranked simulations and the remainder are included in Appendix C.

V. CONCLUSIONS

In this work, we have demonstrated a consolidated and efficient way to perform Bayesian inference on sparsely sampled simulations of compact binary formation with isolated binary evolution, where each simulation provides only a weighted sample of events. We applied our technique to compare a small collection of StarTrack binary evolution simulations to the compact binary population reported by the LIGO/Virgo Collaboration [3,63–65]. Consistent with prior work and with observations of galactic x-ray binaries' proper motions (see, e.g., Table 7 in [25]), we conclude that SN recoil kicks would need to be modest but nonzero to explain the numbers and properties of observed binaries. Previous proof-of-concept studies [54,80] have demonstrated the merger rate and mass distribution to be very effective at discriminating between different evolutionary models within isolated binary evolution. With the increasing number of observed gravitational-wave events as ground-based observatories like LIGO, Virgo, and KAGRA continue to scan the Universe for merging compact binaries, we anticipate this method can enable tight constraints on physical processes within isolated binary evolution [126–129,141,142].

Other groups (including [19,20]) have studied the significance of the two NSBH events observed in the third observing run of the modern ground-based gravitational-wave observatories [13]. We concur with their findings that these observations are essential to constraining the formation of compact objects through isolated binary evolution, and we demonstrate this by considering the strong correlation between SN recoil kicks and NSBH detection rates (see Fig. 7).

Other groups have also developed methods to infer what kinds of binary evolution models are compatible with observations. For example, one investigation [33] involved backward-propagating binaries from their final state to consistent progenitor configurations, recovering ranges for both physical (binary mass and orbit) and binary evolution model parameters. Meanwhile, another group [59] has demonstrated a method for constraining individual assumptions concurrently through iteratively refining a one-dimensional prior for each continuous parameter.

In these and other studies, previous works have highlighted the challenge in thoroughly investigating the many uncertain assumptions implicit in current binary evolution models; see, e.g., the discussion in [33]. That said, by sampling iteratively from an evolving higher-dimensional posterior, we demonstrate that constraints can be drawn on many of the continuously variable parameters (as opposed to assumptions with only discrete settings) at once. Doing so allows us to explore correlations and confounding effects between formation parameters and narrow down the space of our assumptions.

Various groups have carried out the integration of marginalized likelihoods on binary evolution simulations in the past; their methods included drawing samples from the posterior for each event [3,4,26,46,54,143–146],

kernel-density estimates [147], and Gaussian mixture models [148]. Our method for evaluating these marginalized likelihoods offers several technical advantages; we evaluate a well-constrained likelihood model [125,134] for each single-event likelihood, allowing us to integrate over the merger population directly. We can therefore more confidently assess "outlier" events and otherwise make best use of all available simulation data. We can also immediately work with all simulation observables, without worrying about artificially introducing features with a smoothing algorithm. This approach can be applied immediately to other compact binary formation models of comparable sophistication, including models for isolated binary evolution [149,150], dense interacting stellar clusters [151,152], and active galactic nuclei [153].

Our approach contrasts with the other two most widely used approaches in population inference. One long-term robust approach is to eschew a concrete model, constructing a de facto nonparametric distribution for the rate density $\rho(\vec{\lambda})$ versus binary parameters $\vec{\lambda}$ using the observed set of events, the known or search measurable selection biases, and classical statistical techniques. For example, with sufficiently many events, a simple weighted cumulative distribution will approximate the underlying chirp mass distribution [75,154]. Alternatively, *ad hoc* models are also widely used to address broad questions, when overwhelming statistics are not available for a nonparametric approach. For example, if coalescing binary black holes form from an isolated but interacting pair of stars, their initial conditions and interactions could imply the black hole spins are tightly aligned with the orbital angular momentum [70,155–157]; if they form in densely interacting environments, by contrast, the spins will have random orientations. GW measurements will quickly distinguish between these options [158,159], as long as black hole spin magnitudes are not small, as may be the case [26,160]. The mass distribution may have gaps and limits, the underlying physics of supernova [161] or pair instabilities that prevent black hole formation by very massive stars [76]. The mass and spin distributions may provide insight into the supernova central engine and angular momentum transport in massive stars [139,162–165] (modulo caveats due to significant uncertainties in massive binary stars' initial conditions [166,167], binary evolution [67–69,168,169], and stellar wind mass loss [67]).

However, as observations become more informative, each piece of uncertain physics will produce correlated impacts on multiple properties of the observed binary population, which phenomenological or nonparametric approaches will not naturally identify as possessing a common origin. Model-based approaches enable sharper constraints on uncertain astrophysics with broad observational consequences.

Given the substantial modeling uncertainties associated with compact object spins at formation and their alignment, in this work we have only compared compact binary *mass* distributions to StarTrack predictions. Observations of black hole spin magnitudes and misalignments can possibly differentiate between various formation channels and between different physical models of angular momentum transport within a given formation channel [26,54,158,160,170–172]. For the moment, it seems as though LIGO/Virgo/KAGRA black holes form with low spins, indicating efficient angular momentum transport [26,173]. On the other hand, high-mass x-ray binaries may indicate that BHs form with large spins, yet these estimates are being questioned [174]. Tidal spin-up of stars was proposed for high-spinning LIGO/Virgo/KAGRA BHs, yet it is debated whether only the first-born BH can be spun up [160,175], or does the process apply to both merging BHs [176]? Building upon this idea, other groups propose the black hole formed in a binary system will always have small spin, but the second can have large spin due to presupernova spin-up. Practically speaking, however, the model space that must be explored is larger and the observational constraints far tighter when comparing both mass and spin distributions to current observations. We defer a discussion of these degrees of freedom to future work.

Even without considering the GW190521 merger, we find a preference for the global reduction in mass-loss rates due to stellar wind for hydrogen-dominated stars introduced to StarTrack by Belczynski *et al.* in prior work [78] over nonreduced mass-loss rates (see Sec. II A 2). The authors do not suggest that the reduction factor f_{wind1} is the final model for stellar wind; we only demonstrate that it is preferred over no reduction at all. The weak wind phenomenon is still being understood observationally, and Hubble's ULLYSES program will provide spectral analysis of more bright stars formed at lower metallicities in the near future [177,178].

To close, we emphasize the critical need to widely explore all relevant uncertainties. Given the extremely tight constraints soon available and past experience suggesting strong correlations between population synthesis model parameters, inferences based on a limited subspace of model parameters will inevitably be biased, potentially producing highly misleading conclusions about the most significant model parameters Our own study illustrates the potential pitfalls of insufficiently broad exploration: the one-parameter survey that varied only kick velocity suggested that kick velocity could be well constrained away from zero, but failed to reproduce the shape of the observed gravitational-wave population. Because of the many uncertain parameters in all extant models for compact binary formation, care should be taken when drawing strong conclusions about what nature can permit; cf. [179–181].

We have evaluated the marginal likelihood for each of our simulations, with the raw data available in an associated data release [182].

ACKNOWLEDGMENTS

The authors thank Keith Riles, Zoheyr Doctor, Erika Holmbeck, and Tomasz Bulik for useful feedback. R. O. S. and V. D. are supported by NSF AST-1909534 and PHY-2012057. R. O. S., V. D., and A. Y. are supported by NSF-PHY 2012057; R. O. S. is also supported via NSF PHY-1912632 and AST-1909534. V. D. is supported by an appointment to the NASA Postdoctoral Program at the NASA Goddard Space Flight Center administered by Oak Ridge Associated Universities under Contract No. NPP-GSFC-NOV21-0031. D. W. thanks the NSF (PHY-1912649, PHY-2207728) for support. K. B. acknowledges support from the Polish National Science Center (NCN) grant Maestro (2018/30/A/ST9/00050). This material is based upon work supported by NSF's LIGO Laboratory which is a major facility fully funded by the National Science Foundation. This research has made use of data, software and/or web tools obtained from the Gravitational Wave Open Science Center ([183]), a service of LIGO Laboratory, the LIGO Scientific Collaboration, and the Virgo Collaboration. LIGO Laboratory and Advanced LIGO are funded by the U.S. National Science Foundation (NSF) as well as the Science and Technology Facilities Council of the United Kingdom, the Max-Planck-Society, and the State of Niedersachsen/Germany for support of the construction of Advanced LIGO and construction and operation of the GEO600 detector. Additional support for Advanced LIGO was provided by the Australian Research Council. Virgo is funded through the European Gravitational Observatory, by the French Centre National de Recherche Scientifique, the Italian Istituto Nazionale di Fisica Nucleare, and the Dutch Nikhef, with contributions by institutions from Belgium, Germany, Greece, Hungary, Ireland, Japan, Monaco, Poland, Portugal, Spain. The authors are grateful for computational resources provided by the LIGO Laboratory and supported by National Science Foundation Grants No. PHY-0757058 and No. PHY-0823459. We acknowledge software packages used in this publication, including NumPy [184], SciPy [140], Matplotlib [185], Cython [186], Astropy [123,124], and H5PY [187]. This research was done using resources provided by the Open Science Grid [188,189], which is supported by the National Science Foundation Grants No. 2030508 and No. 1836650, and the U.S. Department of Energy's Office of Science.

APPENDIX A: SNR INTERPOLATION

Integrating more than one million samples and estimating the SNR of each sample in a given StarTrack model is computationally expensive. In this section, we discuss a solution to this problem. The SNR function itself uses LALSuite [130] to generate a PSD for a particular observation run. We developed a tool that interpolates the three-dimensional function $\mathrm{SNR} = \mathrm{SNR}_{\mathrm{lal}}(M_{\mathrm{det},A}, M_{\mathrm{det},B}, l(z))$ in a two-dimensional training space, which is much more computationally efficient. Here, $l(z)$ is the luminosity distance, evaluated using Astropy [123,124], with the Planck 2015 cosmology [122].

We start from the relation given by [190]

$$\mathrm{SNR}^2(\lambda) \approx \int df \frac{\hat{h}(f;\lambda)\hat{h}^*(f;\lambda)}{\mathcal{S}_n(h)}, \tag{A1}$$

which yields

$$\mathrm{SNR}(M_{\mathrm{det},A}, M_{\mathrm{det},B}, l(z)) \approx l(z)^{-1}, \tag{A2}$$

which yields

$$\mathrm{SNR}(M_{\mathrm{det},A}, M_{\mathrm{det},B}, l(z')) = \frac{l(z)}{l(z')}\mathrm{SNR}(M_{\mathrm{det},A}, M_{\mathrm{det},B}, l(z)) \tag{A3}$$

for some arbitrary redshifts, z and z'.

The key here is that we do not need to construct a three-dimensional model. We can interpolate in $M_{\mathrm{det},A}$ and $M_{\mathrm{det},B}$, at some reference redshift z_r, and use the ratio of the luminosity distance to evaluate at an arbitrary redshift. In doing so, we construct a function $f(M_{\mathrm{src},A}, M_{\mathrm{src},B}, z)$, which draws from $\mathrm{SNR}_{\mathrm{lal}}(M_{\mathrm{det},A}, M_{\mathrm{det},B}, z_r)$.

We define $f(M_{\mathrm{src},A}, M_{\mathrm{src},B}, z)$ as such,

$$f(M_{\mathrm{src},A}, M_{\mathrm{src},B}, z) = \mathrm{SNR}((z+1)M_{\mathrm{src},A}, (z+1)M_{\mathrm{src},B}, l(z)), \tag{A4}$$

$$f(M_{\mathrm{src},A}, M_{\mathrm{src},B}, z') = \mathrm{SNR}((z'+1)M_{\mathrm{src},A}, (z'+1)M_{\mathrm{src},B}, l(z')). \tag{A5}$$

From (A3), we have

$$\mathrm{SNR}((z+1)M_{\mathrm{src},A}, (z+1)M_{\mathrm{src},B}, l(z)) = \frac{l(z')}{l(z)}\mathrm{SNR}((z+1)M_{\mathrm{src},A}, (z+1)M_{\mathrm{src},B}, l(z')). \tag{A6}$$

By inputting adjusted M_{src} values, we can reference the same detector mass values at a different redshift,

$$f\left(\frac{z+1}{z'+1}M_{\mathrm{src},A}, \frac{z+1}{z'+1}M_{\mathrm{src},B}, z'\right) = \mathrm{SNR}((z+1)M_{\mathrm{src},A}, (z+1)M_{\mathrm{src},B}, l(z')). \tag{A7}$$

Combining (A4), (A6), and (A7) yields

$$f(M_{\mathrm{src},A}, M_{\mathrm{src},B}, z) = \frac{l(z')}{l(z)} f\left(\frac{z+1}{z'+1}M_{\mathrm{src},A}, \frac{z+1}{z'+1}M_{\mathrm{src},B}, z'\right). \tag{A8}$$

Finally, drawing samples from a model trained at fixed z_r is evaluated as such,

$$f(M_{\mathrm{src},A}, M_{\mathrm{src},B}, z) = \frac{l(z_r)}{l(z)}\mathrm{SNR}((z+1)M_{\mathrm{src},A}, (z+1)M_{\mathrm{src},B}, l(z_r)). \tag{A9}$$

We therefore train $\mathrm{SNR}(M_{\mathrm{det},A}, M_{\mathrm{det},B}, l(z_r))$ using a Gaussian process regression model, which only requires a grid in two dimensions.

To perform Gaussian process regression more efficiently, we have implemented a piecewise-polynomial covariance function with compact support [135]. These basis functions are guaranteed to be positive definite, and the covariance between points becomes zero as their distance increases, which are given as $K_{ppD,q}(r)$,

$$K_{ppD,0}(r) = (1-r)_+^j, \tag{A10}$$

$$K_{ppD,1}(r) = (1-r)_+^{j+1}((j+1)r+1), \tag{A11}$$

$$K_{ppD,2}(r) = \frac{(1-r)_+^{j+2}((j^2+4j+3)r^2+(3j+6)r+3)}{3}, \tag{A12}$$

$$K_{ppD,3}(r) = (1-r)_+^{j+3}((j^3+9j^2+23j+15)r^3 + (6j^2+36j+45)r^2 + (15j+45)r+15))/15, \tag{A13}$$

where $j = \lfloor \frac{D}{2} \rfloor + q + 1$, D is the dimensionality of your dataset, and q is chosen such that the sample function is $2q$ times differentiable. We have chosen $q = 1$, and added a white noise kernel as well. We have seen that the sample time for this function scales only with n for high n.

APPENDIX B: PROPERTIES OF THE BOUNDED MULTIVARIATE NORMAL DISTRIBUTION IN FORMATION PARAMETERS

Table III describes the properties of the bounded multivariate normal distribution used to fit the joint likelihood (as seen in Fig. 10). The process of fitting a bounded multivariate normal distribution to a grid of likelihoods is accomplished using methods similar to those outlined for describing the likelihood of individual events (most similar to the low-latency section of [125]). To expound upon this, the parameters of a multivariate normal distribution can be optimized the same way as any other parametric model, and we use SciPy [140] for this optimization, while using a decomposition of the multivariate normal parameters that lends itself well to the guarantee of positive-definite eigenvalues in the covariance. When optimizing this bounded multivariate normal distribution, we must select a subset of our simulation models in order to avoid contaminating our model of the subspace near our local maximum; this is accomplished by fitting the simulations within some range δP of the maximum value of the joint likelihood. At each iteration, this parameter is tuned by hand. In the final iteration, $\delta\mathrm{P} = 7$, which includes the 27 simulations with the highest joint likelihood.

TABLE III. Properties of the bounded multivariate normal distribution fit to models K0100–K0563; μ describes the location of the maximum likelihood for the multivariate normal distribution. σ describes the scale of the distribution. ρ describes the symmetric correlation matrix.

	f_a	β	σ_{eff} (km/s)	f_{wind1}
μ	0.900	0.75	105.5	0.346
σ	0.019	0.18	10.8	0.022
ρ_{f_a}	1	−0.275	0.050	0.271
ρ_β	−0.275	1	0.830	−0.714
$\rho_{\sigma_{\mathrm{eff}}}$	0.050	0.830	1	−0.624
$\rho_{f_{\mathrm{wind1}}}$	0.271	−0.714	−0.624	1

APPENDIX C: PROPERTIES OF THE SIMULATED UNIVERSES

In Table IV, we present the formation parameters, detection rates, and likelihoods for each model in the K series of StarTrack models, using the assumed cosmology. See Sec. II A 2 for the astrophysical assumptions in this series of models. See Table I for details about how the formation parameter space is sampled.

TABLE IV. K series StarTrack models are listed with their formation parameters, detection rates, and likelihoods.

Model	f_a	β	$\sigma_{\rm eff}$	$f_{\rm wind1}$	$f_{\rm wind2}$	$\mu_{\rm BBH}$	$\mu_{\rm BNS}$	$\mu_{\rm NSBH}$	lnL_rate	lnL_shape	lnL_joint
K0100	0.601	0.934	19.913	0.802	1.000	211.283	3.653	12.227	165.865	−220.574	−54.709
K0101	0.760	0.295	240.759	0.882	1.000	5.419	1.101	0.092	110.485	−290.909	−180.424
K0102	0.878	0.080	225.610	0.777	1.000	6.518	0.999	0.116	123.017	−264.868	−141.851
K0103	0.254	0.633	50.807	0.301	1.000	138.841	6.213	5.306	211.830	−227.597	−15.767
K0104	0.341	0.717	87.670	0.848	1.000	42.216	5.498	1.749	224.546	−267.696	−43.150
K0105	0.427	0.379	110.460	0.927	1.000	28.240	5.320	0.946	209.259	−282.192	−72.934
K0106	0.988	0.459	29.083	0.816	1.000	156.488	1.837	9.295	201.870	−203.949	−2.078
K0107	0.658	0.413	62.227	0.510	1.000	73.409	2.355	2.884	234.499	−207.589	26.910
K0108	0.995	0.107	87.611	0.928	1.000	39.839	1.122	1.406	223.854	−190.685	33.169
K0109	0.857	0.868	220.586	0.562	1.000	10.062	1.058	0.141	151.167	−246.722	−95.554
K0110	0.518	0.799	63.414	0.221	1.000	194.346	3.299	3.520	183.153	−189.839	−6.686
K0111	0.837	0.600	110.523	0.449	1.000	44.770	1.519	1.033	227.290	−194.696	32.594
K0112	0.400	0.907	6.392	0.990	1.000	280.023	9.345	15.088	111.152	−244.211	−133.059
K0113	0.840	0.735	134.489	0.360	1.000	61.669	1.526	0.656	232.920	−197.132	35.788
K0114	0.623	0.599	176.117	0.282	1.000	85.225	1.918	0.296	231.488	−223.177	8.311
K0115	0.930	0.712	141.993	0.201	1.000	160.872	1.822	0.828	203.105	−168.504	34.601
K0116	0.708	0.470	264.589	0.998	1.000	3.716	1.036	0.075	84.583	−302.147	−217.563
K0117	0.698	0.360	258.817	0.878	1.000	4.463	1.152	0.066	96.852	−309.380	−212.528
K0118	0.818	0.779	215.791	0.504	1.000	12.007	1.152	0.153	162.164	−239.691	−77.527
K0119	0.638	0.766	74.144	0.856	1.000	48.927	2.511	2.130	229.889	−226.251	3.638
K0120	0.975	0.137	205.057	0.524	1.000	14.315	1.441	0.202	173.186	−243.715	−70.529
K0121	0.420	0.203	62.056	0.824	1.000	63.707	6.444	2.587	231.998	−262.098	−30.100
K0122	0.422	0.832	141.942	0.241	1.000	125.208	3.751	0.605	219.833	−233.219	−13.386
K0123	0.432	0.500	72.667	0.296	1.000	131.169	5.198	2.647	217.337	−216.426	0.911
K0124	0.542	0.201	184.370	0.247	1.000	94.817	2.505	0.229	229.080	−248.005	−18.925
K0125	0.120	0.253	259.971	0.887	1.000	6.401	3.016	0.208	123.111	−355.152	−232.042
K0126	0.278	0.683	199.585	0.242	1.000	76.684	2.681	0.260	232.111	−249.901	−17.789
K0127	0.966	0.852	2.964	0.881	1.000	293.009	1.739	15.343	105.452	−218.271	−112.819
K0128	0.811	0.382	115.960	0.280	1.000	146.279	1.529	0.936	210.930	−167.546	43.384
K0129	0.994	0.183	212.313	0.985	1.000	8.039	1.354	0.145	137.278	−262.915	−125.636
K0130	0.492	0.329	196.025	0.818	1.000	8.636	2.967	0.184	142.225	−320.652	−178.427
K0131	0.299	0.911	103.281	0.206	1.000	166.551	4.452	1.405	199.561	−220.822	−21.262
K0132	0.757	0.466	220.742	0.759	1.000	7.760	1.243	0.112	134.476	−266.972	−132.496
K0133	0.509	0.608	123.076	0.576	1.000	30.387	3.772	0.819	213.087	−258.201	−45.114
K0134	0.345	0.717	85.452	0.636	1.000	45.790	5.386	1.890	226.908	−265.182	−38.274
K0135	0.774	0.987	200.854	0.953	1.000	9.960	1.277	0.144	150.724	−257.088	−106.364
K0136	0.334	0.902	146.602	0.917	1.000	19.829	3.746	0.535	192.356	−290.712	−98.355
K0137	0.866	0.482	138.925	0.578	1.000	23.243	1.424	0.510	200.695	−218.352	−17.656
K0138	0.126	0.604	66.323	0.367	1.000	91.696	5.372	4.614	230.069	−241.981	−11.911
K0139	0.858	0.375	255.772	0.252	1.000	67.898	0.951	0.089	229.823	−217.515	12.307
K0140	0.732	0.437	76.184	0.262	1.000	187.506	2.027	2.382	188.069	−166.696	21.372
K0141	0.286	0.711	139.228	0.552	1.000	25.775	3.796	0.628	205.495	−273.497	−68.002
K0142	0.469	0.923	118.014	0.629	1.000	31.674	3.931	0.799	214.681	−255.871	−41.190
K0143	0.584	0.325	202.481	0.370	1.000	29.438	1.957	0.217	210.203	−273.606	−63.402
K0144	0.740	0.185	148.965	0.996	1.000	15.904	1.937	0.396	180.425	−256.521	−76.095
K0145	0.722	0.963	258.268	0.919	1.000	4.945	1.033	0.081	104.059	−289.058	−184.999
K0146	0.185	0.539	75.549	0.718	1.000	55.267	4.500	2.765	231.387	−259.174	−27.787
K0147	0.666	0.437	114.327	1.000	1.000	26.469	2.539	0.839	207.535	−251.019	−43.484
K0148	0.836	0.197	48.698	0.868	1.000	85.009	1.152	4.009	232.769	−210.831	21.938
K0149	0.531	0.322	195.912	0.759	1.000	8.485	2.706	0.195	141.294	−310.607	−169.313
K0150	0.676	0.997	222.121	0.277	1.000	56.637	1.358	0.110	228.738	−221.301	7.437
K0151	0.253	0.131	157.710	0.607	1.000	16.654	5.186	0.448	181.908	−326.784	−144.876
K0152	0.717	0.009	236.413	0.745	1.000	4.795	1.295	0.099	102.568	−296.817	−194.249
K0153	0.387	0.711	22.399	0.532	1.000	223.545	8.846	13.789	152.920	−240.270	−87.350
K0154	0.458	0.659	146.488	0.870	1.000	18.293	4.011	0.551	187.999	−296.546	−108.547
K0155	0.236	0.886	8.176	0.682	1.000	312.815	11.335	17.618	82.509	−250.244	−167.736

(Table continued)

TABLE IV. *(Continued)*

Model	f_a	β	$\sigma_{\rm eff}$	$f_{\rm wind1}$	$f_{\rm wind2}$	$\mu_{\rm BBH}$	$\mu_{\rm BNS}$	$\mu_{\rm NSBH}$	lnL_rate	lnL_shape	lnL_joint
K0156	0.493	0.923	188.368	0.501	1.000	16.279	2.592	0.228	180.718	−275.658	−94.940
K0157	0.638	0.107	215.702	0.646	1.000	7.308	1.709	0.106	130.663	−306.466	−175.803
K0158	0.616	0.144	152.066	0.520	1.000	20.406	2.466	0.398	193.830	−262.971	−69.140
K0159	0.831	0.974	250.115	0.438	1.000	12.284	0.932	0.102	162.571	−244.073	−81.502
K0160	0.304	0.647	8.399	0.448	1.000	349.060	12.150	17.587	53.510	−248.959	−195.449
K0161	0.975	0.215	171.835	0.695	1.000	13.963	1.496	0.295	172.432	−236.396	−63.964
K0162	0.526	0.680	60.258	0.753	1.000	65.159	4.125	3.082	233.451	−233.016	0.435
K0163	0.300	0.183	206.975	0.340	1.000	8.515	3.342	0.215	141.479	−329.698	−188.219
K0164	0.267	0.213	164.918	0.247	1.000	19.405	4.068	0.440	190.769	−298.721	−107.952
K0165	0.868	0.462	92.669	0.774	1.000	39.957	1.152	1.369	223.955	−197.540	26.415
K0166	0.423	0.213	56.383	0.455	1.000	83.455	6.031	3.533	231.649	−233.765	−2.116
K0167	0.761	0.660	258.164	0.430	1.000	10.968	0.944	0.084	155.363	−257.441	−102.078
K0168	0.357	0.337	193.666	0.923	1.000	10.132	3.560	0.251	152.557	−330.597	−178.041
K0169	0.117	0.555	82.210	0.311	1.000	74.320	5.092	3.419	233.086	−242.142	−9.056
K0170	0.804	0.542	76.286	0.774	1.000	48.011	1.333	2.008	229.360	−201.292	28.069
K0171	0.685	0.446	212.539	0.375	1.000	24.946	1.533	0.165	202.214	−245.408	−43.194
K0172	0.875	0.563	204.763	0.803	1.000	8.613	1.125	0.162	141.725	−267.705	−125.980
K0173	0.943	0.528	224.858	0.630	1.000	8.693	1.195	0.137	142.057	−259.559	−117.502
K0174	0.585	0.801	97.171	0.425	1.000	55.008	2.773	1.398	232.070	−219.620	12.450
K0175	0.457	0.025	236.471	0.297	1.000	12.083	2.646	0.110	162.096	−309.750	−147.654
K0176	0.674	0.346	258.814	0.318	1.000	35.979	1.166	0.068	215.675	−241.848	−26.173
K0177	0.681	0.835	210.384	0.407	1.000	20.650	1.474	0.160	192.819	−246.557	−53.738
K0178	0.773	0.657	55.335	0.737	1.000	75.221	1.578	3.745	234.080	−206.444	27.637
K0179	0.126	0.201	125.836	0.931	1.000	31.239	6.334	1.398	213.191	−305.206	−92.015
K0180	0.722	0.554	147.747	0.961	1.000	17.099	1.884	0.453	184.655	−251.980	−67.325
K0181	0.689	0.253	29.436	0.550	1.000	181.319	2.771	9.507	187.364	−197.223	−9.859
K0182	0.130	0.295	33.345	0.269	1.000	49.020	1.062	0.795	229.025	−202.291	26.734
K0183	0.884	0.269	90.141	0.693	1.000	41.237	1.136	1.414	224.953	−195.859	29.094
K0184	0.306	0.138	114.363	0.751	1.000	28.349	5.609	0.809	209.069	−296.469	−87.400
K0185	0.934	0.586	262.629	0.826	1.000	4.363	0.962	0.085	95.646	−276.863	−181.217
K0186	0.542	0.073	40.379	0.301	1.000	202.739	3.509	6.610	175.888	−183.179	−7.291
K0187	0.945	0.940	219.589	0.737	1.000	9.594	1.175	0.153	148.450	−250.367	−101.917
K0188	0.312	0.319	123.452	0.844	1.000	24.918	4.941	0.730	203.500	−293.207	−89.707
K0189	0.471	0.297	113.126	0.477	1.000	34.661	4.433	0.872	218.022	−262.282	−44.260
K0190	0.318	0.122	65.351	0.988	1.000	58.858	7.194	2.233	230.677	−280.535	−49.858
K0191	0.935	0.683	242.426	0.528	1.000	9.234	1.081	0.121	145.542	−259.596	−114.053
K0192	0.989	0.080	226.087	0.617	1.000	9.224	1.340	0.117	145.591	−261.511	−115.920
K0193	0.562	0.902	153.466	0.685	1.000	21.148	2.717	0.451	195.803	−258.995	−63.193
K0194	0.547	0.243	18.075	0.552	1.000	265.521	5.464	14.762	124.916	−221.470	−96.553
K0195	0.969	0.596	230.153	0.677	1.000	8.185	1.230	0.134	138.216	−259.604	−121.388
K0196	0.799	0.887	142.664	0.712	1.000	21.831	1.577	0.499	197.613	−224.074	−26.461
K0197	0.970	0.245	180.729	0.657	1.000	13.263	1.503	0.251	169.153	−240.993	−71.840
K0198	0.259	0.026	119.346	0.560	1.000	28.400	6.606	0.834	208.512	−304.971	−96.459
K0199	0.622	0.973	82.652	0.403	1.000	72.468	2.238	1.570	234.624	−196.680	37.944
K0200	0.842	0.044	142.101	0.301	1.000	107.759	1.468	0.515	226.651	−178.352	48.299
K0201	0.196	0.136	236.881	0.392	1.000	6.009	3.760	0.176	118.351	−364.097	−245.746
K0202	0.774	0.806	151.638	0.830	1.000	17.888	1.516	0.438	186.996	−239.622	−52.627
K0203	0.638	0.794	134.871	0.892	1.000	20.768	2.419	0.608	195.381	−259.094	−63.714
K0204	0.580	0.324	252.094	0.370	1.000	19.113	1.552	0.084	187.613	−274.474	−86.861
K0205	0.648	0.780	224.738	0.413	1.000	16.827	1.414	0.127	181.454	−261.137	−79.683
K0206	0.835	0.257	30.605	0.687	1.000	163.802	1.763	8.778	198.238	−203.731	−5.492
K0207	0.631	0.158	21.601	0.454	1.000	259.262	3.887	13.470	131.461	−206.505	−75.044
K0208	0.828	0.886	221.788	0.727	1.000	7.989	1.052	0.139	136.600	−255.356	−118.756
K0209	0.307	0.646	7.357	0.350	1.000	380.715	11.946	17.420	28.423	−237.200	−208.778
K0210	0.583	0.508	27.428	0.973	1.000	154.118	4.008	9.340	202.495	−222.565	−20.069
K0211	0.309	0.159	201.028	0.564	1.000	8.656	3.699	0.213	142.349	−340.366	−198.017

(Table continued)

TABLE IV. *(Continued)*

Model	f_a	β	$\sigma_{\rm eff}$	$f_{\rm wind1}$	$f_{\rm wind2}$	$\mu_{\rm BBH}$	$\mu_{\rm BNS}$	$\mu_{\rm NSBH}$	lnL_rate	lnL_shape	lnL_joint
K0212	0.662	0.217	163.568	0.618	1.000	14.786	2.141	0.298	175.823	−275.181	−99.358
K0213	0.359	0.440	54.617	0.993	1.000	68.728	6.743	3.604	231.877	−263.958	−32.081
K0214	0.429	0.410	248.751	0.989	1.000	4.716	2.526	0.093	101.437	−349.241	−247.804
K0215	0.214	0.160	100.103	0.854	1.000	35.115	7.426	1.352	216.941	−305.298	−88.357
K0216	0.601	0.014	113.845	0.234	1.000	162.168	3.002	0.909	202.310	−204.873	−2.563
K0217	0.360	0.259	240.038	0.261	1.000	14.402	2.699	0.104	172.295	−318.473	−146.178
K0218	0.427	0.173	239.510	0.806	1.000	5.014	2.806	0.097	105.559	−352.627	−247.067
K0219	0.935	0.346	262.300	0.401	1.000	15.484	1.031	0.075	175.557	−238.653	−63.096
K0220	0.953	0.055	141.970	0.973	1.000	16.950	1.446	0.436	184.025	−227.515	−43.490
K0221	0.553	0.481	180.226	0.831	1.000	11.246	2.668	0.258	159.321	−304.756	−145.434
K0222	0.900	0.402	108.640	0.688	1.000	33.393	1.317	0.923	217.359	−201.193	16.165
K0223	0.655	0.712	207.210	0.942	1.000	8.172	1.657	0.186	138.882	−291.615	−152.734
K0224	0.338	0.394	80.262	0.751	1.000	46.971	5.967	1.895	227.184	−270.245	−43.061
K0225	0.474	0.217	105.481	0.504	1.000	35.297	4.590	0.980	218.734	−262.636	−43.903
K0226	0.697	0.824	158.286	0.891	1.000	15.788	1.797	0.346	179.785	−260.449	−80.664
K0227	0.361	0.051	57.998	0.784	1.000	70.631	7.503	2.741	231.710	−259.158	−27.447
K0228	0.907	0.404	187.355	0.605	1.000	12.273	1.294	0.227	164.288	−241.288	−77.001
K0229	0.940	0.103	14.977	0.289	1.000	442.513	3.019	18.701	−17.508	−174.222	−191.729
K0230	0.130	0.152	262.077	0.502	1.000	6.081	3.497	0.193	119.408	−391.973	−272.565
K0231	0.797	0.862	220.010	0.899	1.000	8.097	1.081	0.146	137.570	−263.049	−125.479
K0232	0.246	0.177	149.133	0.820	1.000	18.895	5.220	0.516	188.953	−316.220	−127.268
K0233	0.596	0.242	207.870	0.635	1.000	8.643	2.007	0.159	142.185	−300.126	−157.941
K0234	0.151	0.398	245.003	0.892	1.000	7.962	2.359	0.200	137.352	−329.718	−192.366
K0235	0.212	0.382	14.597	0.745	1.000	276.388	13.358	17.507	108.426	−256.416	−147.990
K0236	0.519	0.285	216.788	0.527	1.000	9.242	2.387	0.154	146.326	−300.756	−154.430
K0237	0.579	0.493	78.844	0.339	1.000	101.660	2.963	2.251	229.679	−202.284	27.395
K0238	0.296	0.196	13.690	0.497	1.000	324.644	14.022	15.458	72.990	−249.897	−176.907
K0239	0.664	0.697	110.478	0.994	1.000	29.782	2.509	1.013	212.922	−243.652	−30.729
K0240	0.198	0.165	23.525	0.994	1.000	197.876	14.504	12.111	166.556	−279.413	−112.857
K0241	0.562	0.117	104.468	0.859	1.000	28.172	3.811	0.858	209.888	−261.290	−51.402
K0242	0.399	0.795	252.832	0.725	1.000	5.536	2.343	0.107	112.460	−336.221	−223.761
K0243	0.416	0.546	69.247	0.561	1.000	61.726	5.653	2.683	232.211	−254.436	−22.225
K0244	0.465	0.403	213.558	0.521	1.000	9.571	2.672	0.161	148.542	−309.487	−160.945
K0245	0.826	0.417	152.677	0.801	1.000	16.718	1.347	0.359	182.911	−230.508	−47.597
K0246	0.806	0.776	236.380	0.515	1.000	8.260	1.017	0.107	138.199	−261.755	−123.556
K0247	0.687	0.579	221.184	0.359	1.000	28.691	1.398	0.163	208.461	−240.289	−31.828
K0248	0.322	0.431	95.468	0.931	1.000	37.095	5.562	1.303	220.172	−283.521	−63.349
K0249	0.143	0.087	254.669	0.504	1.000	6.807	3.964	0.191	126.578	−386.876	−260.298
K0250	0.678	0.331	120.711	0.660	1.000	27.245	2.446	0.702	208.638	−239.217	−30.578
K0251	0.640	0.268	254.375	0.278	1.000	49.266	1.362	0.087	225.626	−252.686	−27.059
K0252	0.575	0.578	210.856	0.601	1.000	9.772	1.964	0.171	150.034	−293.436	−143.402
K0253	0.687	0.858	76.876	0.518	1.000	58.727	2.157	2.143	233.284	−204.180	29.104
K0254	0.236	0.932	32.523	0.755	1.000	143.551	6.840	7.942	207.259	−246.995	−39.736
K0255	0.451	0.787	57.284	0.203	1.000	219.635	4.676	4.513	165.496	−199.079	−33.583
K0256	0.117	0.987	81.347	0.360	1.000	124.126	4.254	2.499	220.982	−207.053	13.929
K0257	0.957	0.506	212.720	0.654	1.000	8.835	1.292	0.163	143.458	−250.874	−107.416
K0258	0.890	0.189	82.475	0.552	1.000	50.322	1.215	1.661	230.334	−190.054	40.280
K0259	0.875	0.397	254.153	0.717	1.000	4.725	0.884	0.082	100.860	−265.681	−164.821
K0260	0.403	0.562	117.839	0.231	1.000	149.543	4.453	1.033	208.569	−227.324	−18.755
K0261	0.241	0.830	91.406	0.474	1.000	53.597	4.055	1.754	231.185	−242.893	−11.708
K0262	0.563	0.324	228.116	0.414	1.000	13.048	1.812	0.112	166.778	−282.392	−115.614
K0263	0.844	0.410	216.207	0.976	1.000	6.583	1.050	0.142	124.099	−266.389	−142.290
K0264	0.948	0.744	110.478	0.781	1.000	30.935	1.274	1.037	214.407	−200.147	14.260
K0265	0.514	0.818	89.526	0.610	1.000	44.405	3.911	1.648	226.884	−239.466	−12.582
K0266	0.433	0.432	246.958	0.204	1.000	75.373	2.276	0.111	230.697	−270.214	−39.517
K0267	0.752	0.434	39.461	0.900	1.000	107.098	2.037	5.718	226.567	−211.798	14.769

(Table continued)

TABLE IV. *(Continued)*

Model	f_a	β	$\sigma_{\rm eff}$	$f_{\rm wind1}$	$f_{\rm wind2}$	$\mu_{\rm BBH}$	$\mu_{\rm BNS}$	$\mu_{\rm NSBH}$	lnL_rate	lnL_shape	lnL_joint
K0268	0.286	0.996	115.789	0.940	1.000	31.879	3.730	0.839	215.093	−264.262	−49.169
K0269	0.280	0.793	192.480	0.770	1.000	11.509	2.655	0.291	160.937	−304.922	−143.985
K0270	0.550	0.062	123.075	0.424	1.000	34.995	3.458	0.655	218.501	−257.066	−38.565
K0271	0.788	0.780	141.167	0.905	1.000	19.615	1.481	0.525	192.170	−232.537	−40.367
K0272	0.520	0.423	99.607	0.230	1.000	168.108	3.717	1.354	199.025	−209.412	−10.388
K0273	0.221	0.003	70.808	0.993	1.000	55.174	11.035	2.508	226.680	−315.415	−88.736
K0274	0.526	0.628	142.634	0.377	1.000	44.467	3.046	0.513	226.088	−248.370	−22.282
K0275	0.257	0.841	26.537	0.728	1.000	175.442	8.604	10.678	186.363	−247.377	−61.013
K0276	0.811	0.333	128.757	0.934	1.000	21.170	1.504	0.600	196.305	−226.918	−30.613
K0277	0.885	0.625	2.921	0.295	1.000	443.836	2.203	15.234	−15.373	−196.146	−211.519
K0278	0.377	0.731	95.169	0.935	1.000	36.140	5.107	1.426	219.591	−276.970	−57.379
K0279	0.211	0.516	155.817	0.778	1.000	18.298	2.808	0.546	188.492	−285.684	−97.192
K0280	0.832	0.535	21.723	0.998	1.000	187.980	2.444	11.915	181.420	−208.164	−26.744
K0281	0.599	0.476	18.125	0.537	1.000	262.313	4.306	15.493	127.296	−208.347	−81.051
K0282	0.429	0.294	31.524	0.651	1.000	155.250	7.291	8.276	200.625	−230.816	−30.191
K0283	0.507	0.909	263.904	0.978	1.000	4.523	1.912	0.069	98.107	−335.761	−237.654
K0284	0.479	0.007	225.259	0.336	1.000	10.927	2.654	0.122	156.217	−308.565	−152.348
K0285	0.336	0.215	23.108	0.592	1.000	220.868	11.044	11.443	154.948	−243.512	−88.563
K0286	0.972	0.091	203.594	0.881	1.000	8.101	1.336	0.154	137.875	−261.822	−123.947
K0287	0.841	0.332	117.838	0.729	1.000	25.896	1.350	0.778	206.370	−209.516	−3.146
K0288	0.176	0.196	113.997	0.516	1.000	34.931	6.651	1.333	217.293	−298.982	−81.689
K0289	0.232	0.638	170.940	0.404	1.000	20.120	2.708	0.400	193.057	−274.791	−81.734
K0290	0.239	0.937	230.724	0.699	1.000	9.754	1.794	0.139	149.526	−295.921	−146.395
K0291	0.204	0.116	190.383	0.860	1.000	10.821	5.074	0.294	156.080	−351.623	−195.543
K0292	0.226	0.759	212.069	0.205	1.000	90.492	2.033	0.237	230.156	−243.258	−13.103
K0293	0.267	0.680	234.693	0.778	1.000	6.763	2.008	0.159	126.413	−323.326	−196.913
K0294	0.368	0.671	79.972	0.626	1.000	50.760	5.622	2.167	229.203	−259.798	−30.595
K0295	0.485	0.172	204.160	0.842	1.000	7.605	3.197	0.157	133.742	−334.757	−201.016
K0296	0.775	0.684	190.811	0.944	1.000	10.318	1.341	0.248	153.932	−257.934	−104.002
K0297	0.872	0.702	187.288	0.897	1.000	9.985	1.185	0.237	151.735	−244.579	−92.844
K0298	0.112	0.522	132.286	0.305	1.000	36.931	3.855	1.358	221.019	−260.956	−39.938
K0299	0.948	0.792	54.970	0.716	1.000	75.027	1.069	3.810	233.788	−207.933	25.854
K0300	0.263	0.374	73.747	0.277	1.000	73.447	5.804	2.643	232.919	−244.557	−11.637
K0301	0.703	0.830	116.710	0.219	1.000	166.068	2.062	0.912	200.313	−182.996	17.318
K0302	0.686	0.763	93.008	0.637	1.000	41.287	2.311	1.402	225.230	−219.557	5.673
K0303	0.399	0.649	95.903	0.732	1.000	37.621	5.257	1.459	220.922	−268.947	−48.025
K0304	0.224	0.043	59.048	0.875	1.000	71.430	10.456	3.284	229.250	−289.179	−59.929
K0305	0.178	0.449	99.626	0.359	1.000	50.605	4.306	1.803	229.917	−251.058	−21.142
K0306	0.590	0.880	159.743	0.251	1.000	103.292	2.176	0.405	227.780	−218.358	9.422
K0307	0.235	0.965	239.906	0.614	1.000	9.019	1.657	0.135	144.545	−297.306	−152.761
K0308	0.338	0.432	60.773	0.418	1.000	80.202	6.356	3.506	231.831	−247.765	−15.933
K0309	0.850	0.773	142.568	0.967	1.000	17.616	1.432	0.502	186.343	−235.484	−49.141
K0310	0.184	0.563	179.068	0.745	1.000	15.177	2.300	0.410	177.820	−287.522	−109.703
K0311	0.641	0.688	150.912	0.803	1.000	17.276	2.162	0.451	185.210	−262.672	−77.462
K0312	0.592	0.597	32.770	0.695	1.000	140.958	3.044	8.170	210.545	−212.709	−2.164
K0313	0.994	0.900	204.913	0.577	1.000	13.872	1.406	0.200	171.335	−242.480	−71.145
K0314	0.213	0.342	39.145	0.819	1.000	97.051	7.810	6.564	225.866	−269.540	−43.674
K0315	0.811	0.711	134.412	0.841	1.000	20.968	1.441	0.587	195.765	−221.824	−26.058
K0316	0.428	0.094	49.986	0.873	1.000	81.245	3.647	3.403	233.360	−239.624	−6.264
K0317	0.733	0.972	258.924	0.694	1.000	5.979	0.972	0.079	116.600	−270.721	−154.121
K0318	0.674	0.937	39.901	0.495	1.000	126.263	2.116	5.847	219.167	−195.860	23.307
K0319	0.852	0.670	192.882	0.366	1.000	32.806	1.277	0.249	214.702	−213.178	1.525
K0320	0.731	0.541	150.099	0.322	1.000	77.547	1.834	0.492	233.185	−203.531	29.654
K0321	0.652	0.197	113.049	0.413	1.000	49.187	2.603	0.777	229.327	−222.643	6.684
K0322	0.544	0.497	246.851	0.600	1.000	5.945	1.782	0.102	117.113	−316.831	−199.718
K0323	0.885	0.108	17.025	0.891	1.000	240.566	2.445	13.569	145.199	−213.594	−68.395

(Table continued)

TABLE IV. *(Continued)*

Model	f_a	β	$\sigma_{\rm eff}$	$f_{\rm wind1}$	$f_{\rm wind2}$	$\mu_{\rm BBH}$	$\mu_{\rm BNS}$	$\mu_{\rm NSBH}$	lnL_rate	lnL_shape	lnL_joint
K0324	0.566	0.847	175.416	0.200	1.000	117.061	2.195	0.357	222.813	−218.514	4.299
K0325	0.736	0.650	255.738	0.912	1.000	4.791	1.060	0.085	102.070	−290.311	−188.241
K0326	0.269	0.789	50.607	0.909	1.000	76.427	5.745	4.278	232.170	−263.993	−31.823
K0327	0.709	0.174	179.055	0.715	1.000	12.141	1.818	0.250	163.969	−264.727	−100.758
K0328	0.842	0.142	191.682	0.360	1.000	43.663	1.255	0.189	223.926	−221.081	2.845
K0329	0.178	0.956	157.050	0.493	1.000	28.500	2.303	0.481	210.113	−244.758	−34.645
K0330	0.353	0.771	104.538	0.331	1.000	85.087	4.694	1.286	232.474	−237.973	−5.499
K0331	0.109	0.577	100.440	0.611	1.000	46.866	4.612	2.353	227.943	−262.346	−34.403
K0332	0.897	0.765	219.311	0.244	1.000	82.514	1.242	0.223	231.184	−212.517	18.667
K0333	0.747	0.977	114.264	0.480	1.000	38.554	1.921	0.770	222.486	−208.767	13.718
K0334	0.265	0.977	32.650	0.470	1.000	163.047	6.825	8.042	196.867	−235.057	−38.190
K0335	0.714	0.142	43.828	0.381	1.000	142.678	2.208	5.874	211.527	−190.218	21.310
K0336	0.247	0.738	167.015	0.837	1.000	15.137	2.706	0.382	177.476	−285.410	−107.934
K0337	0.485	0.435	235.220	0.273	1.000	58.723	2.246	0.112	229.408	−267.467	−38.059
K0338	0.798	0.616	176.203	0.353	1.000	47.704	1.356	0.284	227.029	−204.527	22.502
K0339	0.952	0.704	211.852	0.919	1.000	7.867	1.167	0.150	135.848	−257.044	−121.196
K0340	0.652	0.080	78.974	0.880	1.000	47.205	2.844	1.534	228.888	−231.161	−2.273
K0341	0.478	0.784	70.920	0.785	1.000	53.091	4.892	2.473	230.514	−247.773	−17.258
K0342	0.570	0.169	216.986	0.703	1.000	6.574	1.860	0.140	124.322	−307.691	−183.369
K0343	0.775	0.952	249.137	0.626	1.000	7.508	1.041	0.089	131.764	−261.177	−129.414
K0344	0.909	0.546	167.454	0.391	1.000	36.703	1.433	0.398	219.750	−201.444	18.306
K0345	0.153	0.818	65.304	0.741	1.000	78.374	4.469	3.683	233.103	−242.341	−9.238
K0346	0.394	0.255	30.174	0.335	1.000	220.366	7.873	10.214	158.783	−217.760	−58.977
K0347	0.150	0.850	117.918	0.247	1.000	142.160	3.364	1.373	213.064	−211.769	1.295
K0348	0.308	0.209	110.231	0.947	1.000	28.180	5.597	0.857	208.883	−292.924	−84.041
K0349	0.673	0.302	169.502	0.590	1.000	15.502	2.067	0.283	178.425	−267.194	−88.769
K0350	0.387	0.984	115.792	0.331	1.000	81.943	4.222	0.831	232.748	−234.223	−1.475
K0351	0.203	0.361	95.381	0.818	1.000	39.774	4.881	1.604	223.048	−277.884	−54.836
K0352	0.853	0.403	18.704	0.430	1.000	286.973	2.618	16.061	109.301	−194.099	−84.798
K0353	0.694	0.685	128.466	0.547	1.000	28.201	2.165	0.651	210.103	−229.812	−19.709
K0354	0.800	0.542	25.926	0.843	1.000	172.098	2.245	10.312	192.290	−221.290	−29.000
K0355	0.295	0.421	127.341	0.795	1.000	24.529	4.397	0.755	203.109	−289.782	−86.673
K0356	0.998	0.311	212.253	0.562	1.000	11.535	1.467	0.169	160.104	−254.176	−94.071
K0357	0.958	0.703	243.422	0.951	1.000	5.793	1.080	0.112	115.273	−269.123	−153.850
K0358	0.861	0.249	128.511	0.331	1.000	92.076	1.340	0.634	231.253	−175.785	55.468
K0359	0.750	0.767	42.966	0.719	1.000	99.329	1.777	5.475	229.057	−207.574	21.483
K0360	0.743	0.020	141.951	0.329	1.000	80.119	1.946	0.452	232.841	−200.927	31.914
K0361	0.462	0.313	130.827	0.479	1.000	27.107	4.235	0.625	207.566	−269.451	−61.885
K0363	0.722	0.597	250.456	0.387	1.000	17.078	1.087	0.124	182.030	−244.110	−62.079
K0364	0.855	0.063	166.583	0.723	1.000	13.056	1.341	0.230	168.007	−239.512	−71.505
K0365	0.744	0.906	176.416	0.819	1.000	13.666	1.436	0.275	171.037	−247.814	−76.776
K0366	0.186	0.107	207.694	0.772	1.000	9.495	4.753	0.252	147.913	−361.774	−213.861
K0367	0.787	0.434	93.808	0.246	1.000	188.000	1.573	1.492	187.665	−160.323	27.342
K0368	0.433	0.098	229.431	0.619	1.000	5.680	2.944	0.127	114.341	−338.469	−224.127
K0370	0.762	0.633	206.376	0.754	1.000	8.662	1.259	0.179	142.366	−266.043	−123.677
K0371	0.495	0.679	82.476	0.307	1.000	122.817	4.183	2.156	221.613	−212.038	9.575
K0373	0.992	0.046	47.437	0.565	1.000	101.372	1.220	4.922	228.624	−192.698	35.926
K0374	0.272	0.181	34.634	0.266	1.000	209.223	9.689	8.931	165.803	−226.200	−60.398
K0375	0.880	0.248	199.772	0.878	1.000	8.893	1.081	0.168	143.782	−249.975	−106.192
K0377	0.812	0.227	189.990	0.887	1.000	9.752	1.277	0.178	149.809	−256.097	−106.289
K0380	0.549	0.597	34.127	0.347	1.000	188.641	3.378	8.511	183.456	−195.869	−12.413
K0381	0.909	0.595	163.142	0.211	1.000	147.292	1.567	0.509	209.633	−178.197	31.436
K0382	0.675	0.071	32.952	0.780	1.000	136.917	2.747	7.188	213.309	−220.948	−7.639
K0383	0.123	0.991	123.925	0.879	1.000	50.161	3.126	1.009	229.899	−231.510	−1.610
K0384	0.601	0.120	37.885	0.535	1.000	133.607	2.918	6.689	215.161	−213.790	1.372
K0385	0.275	0.768	42.060	0.592	1.000	107.895	6.492	6.033	223.959	−257.403	−33.444

(Table continued)

TABLE IV. *(Continued)*

Model	f_a	β	$\sigma_{\rm eff}$	$f_{\rm wind1}$	$f_{\rm wind2}$	$\mu_{\rm BBH}$	$\mu_{\rm BNS}$	$\mu_{\rm NSBH}$	lnL_rate	lnL_shape	lnL_joint
K0387	0.562	0.293	75.549	0.475	1.000	58.357	3.307	2.130	232.904	−227.631	5.273
K0389	0.150	0.382	197.033	0.971	1.000	11.644	3.126	0.413	162.073	−321.357	−159.284
K0390	0.681	0.440	263.867	0.473	1.000	8.537	1.092	0.065	139.421	−289.268	−149.847
K0392	0.707	0.065	124.780	0.361	1.000	67.310	2.396	0.660	233.621	−216.719	16.902
K0400	0.798	0.814	63.567	0.220	1.000	212.642	1.478	3.349	171.622	−163.739	7.883
K0401	0.865	0.549	54.870	0.636	1.000	77.514	1.304	3.749	233.840	−201.968	31.872
K0402	0.870	0.689	87.462	0.331	1.000	110.898	1.331	1.866	226.745	−165.017	61.727
K0403	0.834	0.232	105.313	0.826	1.000	30.279	1.408	0.951	213.499	−209.558	3.941
K0404	0.578	0.275	51.454	0.624	1.000	85.105	2.943	3.864	232.910	−218.068	14.842
K0405	0.831	0.434	144.720	0.867	1.000	18.006	1.368	0.480	187.434	−228.955	−41.520
K0406	0.730	0.398	149.619	0.749	1.000	17.332	1.949	0.404	185.223	−250.020	−64.797
K0407	0.516	0.205	82.658	0.579	1.000	47.494	4.331	1.619	228.415	−243.420	−15.006
K0408	0.649	0.556	105.290	0.324	1.000	100.542	2.464	1.145	229.885	−198.792	31.093
K0409	0.898	0.429	45.409	0.836	1.000	90.896	1.266	4.638	231.440	−210.217	21.222
K0410	0.939	0.028	102.768	0.817	1.000	31.067	1.283	0.941	214.488	−198.815	15.673
K0411	0.816	0.591	20.698	0.304	1.000	342.564	2.690	16.346	66.192	−183.133	−116.942
K0412	0.673	0.451	106.231	0.208	1.000	193.043	2.409	1.197	184.399	−181.782	2.617
K0413	0.835	0.541	115.028	0.525	1.000	35.394	1.332	0.883	219.507	−196.920	22.586
K0414	0.586	0.930	87.034	0.977	1.000	41.246	3.008	1.397	225.028	−231.323	−6.295
K0415	0.549	0.123	100.110	0.238	1.000	165.017	3.459	1.201	200.807	−208.365	−7.558
K0416	0.691	0.176	31.915	0.568	1.000	160.910	2.829	8.374	200.038	−206.232	−6.194
K0417	0.924	0.404	149.630	0.340	1.000	74.944	1.549	0.512	233.336	−184.708	48.628
K0418	0.740	0.582	108.808	0.969	1.000	28.179	1.959	0.940	210.520	−231.438	−20.919
K0419	0.526	0.221	57.959	0.724	1.000	71.702	4.318	2.983	233.730	−235.581	−1.851
K0420	0.859	0.762	66.496	0.516	1.000	64.029	1.233	2.784	233.893	−193.844	40.049
K0421	0.753	0.259	85.405	0.384	1.000	75.886	1.877	1.634	234.549	−187.801	46.748
K0422	0.836	0.460	85.993	0.305	1.000	134.442	1.278	1.807	217.029	−161.484	55.545
K0423	0.581	0.288	107.868	0.609	1.000	32.555	3.253	0.886	216.195	−251.335	−35.140
K0424	0.957	0.496	119.264	0.933	1.000	26.891	1.417	0.836	208.204	−211.055	−2.852
K0425	0.733	0.912	88.498	0.377	1.000	74.659	1.907	1.562	234.586	−188.861	45.725
K0426	0.917	0.455	39.048	0.883	1.000	104.224	1.525	6.048	227.197	−219.749	7.448
K0427	0.958	0.304	109.713	0.497	1.000	41.096	1.365	1.010	224.717	−186.599	38.118
K0428	0.958	0.222	92.048	0.905	1.000	36.634	1.162	1.286	220.991	−193.849	27.142
K0429	0.557	0.010	35.303	0.340	1.000	204.490	3.446	7.877	173.866	−189.497	−15.631
K0430	0.564	0.770	94.818	0.825	1.000	37.055	3.293	1.402	221.402	−246.536	−25.134
K0431	0.895	0.580	145.037	0.725	1.000	18.099	1.368	0.528	187.857	−222.120	−34.263
K0432	0.856	0.197	136.300	0.870	1.000	19.550	1.334	0.498	191.857	−222.013	−30.156
K0433	0.898	0.253	99.565	0.438	1.000	50.597	1.325	1.199	230.325	−182.549	47.776
K0434	0.534	0.886	99.884	0.492	1.000	46.014	3.342	1.386	228.008	−232.219	−4.211
K0435	0.735	0.256	139.093	0.706	1.000	19.314	2.045	0.461	191.242	−242.585	−51.342
K0436	0.523	0.799	135.428	0.346	1.000	63.442	2.970	0.664	233.092	−231.367	1.725
K0437	0.756	0.641	39.092	0.843	1.000	109.113	2.031	6.258	225.535	−221.091	4.444
K0438	0.578	0.604	133.601	0.842	1.000	20.563	3.065	0.620	194.727	−269.161	−74.434
K0439	0.611	0.616	55.216	0.384	1.000	107.436	2.351	4.128	227.367	−195.320	32.046
K0440	0.554	1.000	94.259	0.923	1.000	36.300	3.384	1.135	220.483	−241.941	−21.459
K0441	0.559	0.399	36.421	0.889	1.000	117.834	3.881	6.510	221.622	−234.795	−13.173
K0442	0.974	0.428	51.110	0.368	1.000	128.115	1.304	4.871	218.818	−179.125	39.694
K0443	0.651	0.017	27.434	0.668	1.000	183.940	3.196	9.368	185.747	−214.008	−28.261
K0444	0.703	0.691	28.625	0.656	1.000	169.291	2.924	9.865	194.120	−209.202	−15.082
K0445	0.877	0.129	54.069	0.992	1.000	70.212	0.949	3.293	233.934	−193.765	40.169
K0446	0.757	0.543	102.587	0.476	1.000	44.131	1.787	1.116	227.022	−204.621	22.401
K0447	0.560	0.195	72.393	0.600	1.000	55.769	3.573	2.088	232.117	−228.917	3.200
K0448	0.552	0.302	97.762	0.636	1.000	35.814	3.824	1.195	219.846	−248.282	−28.436
K0449	0.524	0.538	89.802	0.616	1.000	42.895	3.943	1.554	225.864	−246.465	−20.601
K0450	0.644	0.527	44.776	0.545	1.000	98.084	2.342	4.989	229.681	−215.015	14.665
K0451	0.520	0.071	69.111	0.909	1.000	52.608	4.811	1.963	230.435	−248.848	−18.413

(Table continued)

TABLE IV. *(Continued)*

Model	f_a	β	$\sigma_{\rm eff}$	$f_{\rm wind1}$	$f_{\rm wind2}$	$\mu_{\rm BBH}$	$\mu_{\rm BNS}$	$\mu_{\rm NSBH}$	lnL_rate	lnL_shape	lnL_joint
K0452	0.711	0.910	43.742	0.502	1.000	109.511	1.980	5.313	226.016	−206.819	19.198
K0453	0.804	0.226	98.206	0.440	1.000	50.644	1.515	1.252	230.457	−190.673	39.784
K0454	0.800	0.663	136.610	0.926	1.000	21.033	1.530	0.587	195.954	−230.301	−34.347
K0455	0.743	0.944	125.948	0.706	1.000	26.497	1.835	0.617	207.245	−223.780	−16.534
K0456	0.860	0.711	108.182	0.963	1.000	30.841	1.429	1.019	214.340	−215.070	−0.730
K0457	0.871	0.901	48.681	0.999	1.000	76.872	1.181	4.161	233.604	−199.836	33.768
K0458	0.685	0.896	103.612	0.602	1.000	39.039	2.160	1.052	223.239	−220.475	2.764
K0459	0.725	0.827	142.748	0.580	1.000	24.090	1.854	0.505	202.509	−232.216	−29.707
K0461	0.714	0.708	52.091	0.447	1.000	96.375	2.015	4.557	230.401	−208.420	21.982
K0463	0.763	0.472	104.294	0.953	1.000	32.167	1.819	1.031	216.149	−223.732	−7.584
K0464	0.670	0.560	84.373	0.342	1.000	101.150	2.480	1.969	229.968	−195.650	34.319
K0465	0.730	0.472	69.690	0.269	1.000	178.319	1.894	2.769	193.550	−173.753	19.796
K0466	0.547	0.121	23.959	0.689	1.000	213.230	5.136	10.856	164.910	−220.411	−55.501
K0467	0.760	0.417	55.909	0.214	1.000	243.767	1.588	4.636	149.729	−163.795	−14.066
K0468	0.670	0.260	120.188	0.637	1.000	28.054	2.455	0.690	209.913	−241.681	−31.768
K0469	0.864	0.210	149.204	0.450	1.000	28.829	1.320	0.462	210.419	−213.762	−3.343
K0470	0.626	0.801	33.427	0.376	1.000	177.358	2.526	8.713	190.414	−196.184	−5.770
K0471	0.901	0.005	123.476	0.771	1.000	23.006	1.187	0.589	200.278	−208.959	−8.681
K0472	0.607	0.858	130.083	0.647	1.000	25.873	2.538	0.660	206.191	−244.822	−38.631
K0473	0.843	0.034	149.485	0.330	1.000	83.200	1.464	0.424	232.289	−187.519	44.769
K0474	0.690	0.312	94.298	0.754	1.000	37.180	2.385	1.283	221.725	−232.247	−10.522
K0476	0.622	0.708	137.257	0.954	1.000	19.255	2.478	0.545	191.283	−263.110	−71.827
K0477	0.506	0.128	109.821	0.962	1.000	25.906	4.675	0.783	205.554	−279.501	−73.947
K0478	0.549	0.809	30.572	0.858	1.000	141.297	4.044	8.178	209.940	−231.256	−21.316
K0479	0.848	0.730	107.538	0.270	1.000	142.400	1.482	1.195	213.088	−166.349	46.739
K0480	0.879	0.395	145.811	0.828	1.000	18.688	1.277	0.455	189.304	−224.038	−34.734
K0481	0.699	0.880	95.567	0.477	1.000	47.573	2.113	1.297	229.116	−210.104	19.013
K0482	0.527	0.233	69.517	0.673	1.000	55.126	4.301	2.220	231.559	−237.657	−6.098
K0483	0.921	0.892	118.709	0.326	1.000	91.772	1.471	0.918	231.831	−169.830	62.001
K0484	0.835	0.274	74.132	0.885	1.000	48.323	1.267	1.919	229.477	−201.836	27.641
K0485	0.604	0.624	95.447	0.667	1.000	38.476	2.916	1.333	222.793	−237.013	−14.221
K0486	0.670	0.699	131.431	0.777	1.000	23.245	2.173	0.624	201.086	−245.431	−44.346
K0487	0.927	0.525	127.957	0.686	1.000	26.899	1.330	0.744	208.035	−208.536	−0.500
K0488	0.529	0.094	94.943	0.237	1.000	166.222	3.913	1.330	199.993	−209.608	−9.615
K0489	0.598	0.082	85.001	0.220	1.000	194.832	2.948	1.786	183.350	−188.217	−4.867
K0490	0.515	0.757	114.037	0.853	1.000	28.332	4.015	0.965	210.165	−268.425	−58.260
K0491	0.636	0.293	55.397	0.259	1.000	201.229	2.443	4.186	178.712	−177.382	1.329
K0492	0.771	0.499	85.981	0.780	1.000	42.416	1.723	1.620	226.116	−206.694	19.422
K0493	0.909	0.392	62.222	0.600	1.000	67.899	1.154	3.098	234.095	−190.107	43.987
K0494	0.957	0.807	142.899	0.834	1.000	21.261	1.437	0.530	196.322	−218.058	−21.736
K0495	0.510	0.227	23.302	0.832	1.000	199.574	6.286	10.423	173.407	−229.855	−56.448
K0496	0.679	0.832	61.074	0.713	1.000	65.100	2.119	3.091	234.116	−211.426	22.690
K0497	0.740	0.584	95.682	0.804	1.000	38.916	2.039	1.318	223.326	−218.603	4.723
K0498	0.605	0.438	135.171	0.263	1.000	137.034	2.575	0.640	215.006	−212.649	2.357
K0499	0.667	0.787	59.934	0.966	1.000	63.870	2.266	2.974	233.999	−217.670	16.329
K0500	0.878	0.495	86.170	0.395	1.000	75.533	1.277	1.727	234.414	−178.191	56.223
K0501	0.900	0.459	92.727	0.375	1.000	76.030	1.293	1.471	234.333	−175.368	58.965
K0502	0.907	0.460	77.162	0.412	1.000	78.421	1.234	2.267	234.206	−178.158	56.048
K0503	0.910	0.467	84.408	0.398	1.000	67.148	1.254	1.851	234.328	−176.239	58.089
K0504	0.917	0.473	89.998	0.379	1.000	81.750	1.324	1.655	233.904	−169.629	64.275
K0505	0.954	0.410	72.829	0.456	1.000	71.118	1.183	2.414	234.417	−176.758	57.659
K0506	0.898	0.459	92.364	0.353	1.000	92.756	1.317	1.557	231.964	−164.848	67.117
K0507	0.909	0.519	85.657	0.396	1.000	73.003	1.267	1.951	234.505	−179.194	55.311
K0508	0.923	0.384	77.114	0.393	1.000	82.236	1.205	2.249	233.795	−173.358	60.437
K0509	0.921	0.507	84.399	0.390	1.000	79.392	1.315	2.027	234.183	−179.268	54.916
K0510	0.911	0.403	68.241	0.388	1.000	88.969	1.157	2.788	232.585	−173.426	59.159

(Table continued)

TABLE IV. *(Continued)*

Model	f_a	β	$\sigma_{\rm eff}$	$f_{\rm wind1}$	$f_{\rm wind2}$	$\mu_{\rm BBH}$	$\mu_{\rm BNS}$	$\mu_{\rm NSBH}$	lnL_rate	lnL_shape	lnL_joint
K0511	0.921	0.435	73.476	0.393	1.000	82.475	1.244	2.552	233.739	−173.166	60.573
K0512	0.936	0.416	70.273	0.415	1.000	81.154	1.189	2.792	233.802	−179.155	54.647
K0513	0.918	0.410	78.420	0.399	1.000	79.712	1.179	2.139	234.066	−172.606	61.460
K0514	0.930	0.462	79.502	0.396	1.000	80.282	1.204	2.151	234.026	−173.778	60.248
K0515	0.951	0.429	79.152	0.396	1.000	78.784	1.268	2.222	234.201	−174.505	59.696
K0516	0.920	0.452	76.014	0.377	1.000	93.275	1.221	2.458	231.804	−172.485	59.318
K0517	0.927	0.430	78.398	0.425	1.000	69.391	1.200	2.126	234.419	−176.947	57.472
K0518	0.914	0.439	89.272	0.376	1.000	82.669	1.244	1.750	233.762	−168.977	64.785
K0519	0.929	0.419	76.247	0.406	1.000	80.437	1.140	2.336	233.944	−173.122	60.822
K0520	0.872	0.699	106.028	0.385	1.000	64.455	1.399	1.217	233.943	−175.191	58.752
K0521	0.866	0.960	108.271	0.358	1.000	74.361	1.419	0.980	234.143	−175.519	58.624
K0522	0.900	0.736	112.798	0.359	1.000	71.933	1.449	1.010	234.222	−177.272	56.950
K0523	0.887	0.806	107.927	0.361	1.000	72.813	1.465	1.112	234.314	−176.390	57.925
K0524	0.876	0.867	103.613	0.352	1.000	79.303	1.414	1.243	234.044	−167.049	66.995
K0525	0.939	0.878	118.235	0.364	1.000	70.675	1.441	1.005	234.202	−177.622	56.580
K0526	0.857	0.973	108.823	0.333	1.000	83.641	1.484	1.005	233.380	−171.723	61.656
K0527	0.884	0.598	96.190	0.376	1.000	71.887	1.320	1.469	234.455	−175.695	58.761
K0528	0.887	0.642	97.490	0.358	1.000	83.481	1.407	1.397	233.639	−173.132	60.507
K0529	0.903	0.898	128.786	0.292	1.000	110.820	1.545	0.781	226.199	−168.533	57.666
K0530	0.902	0.820	117.798	0.314	1.000	98.032	1.539	0.958	230.388	−170.850	59.538
K0531	0.919	0.848	120.943	0.320	1.000	92.797	1.513	0.996	231.704	−168.181	63.522
K0532	0.898	0.982	121.847	0.328	1.000	82.013	1.484	0.805	233.350	−175.063	58.287
K0533	0.899	0.778	108.206	0.336	1.000	92.579	1.412	1.111	231.819	−167.581	64.238
K0534	0.907	0.924	112.504	0.316	1.000	96.203	1.437	1.065	230.931	−165.458	65.473
K0535	0.893	0.793	113.454	0.307	1.000	110.340	1.498	1.096	226.714	−166.023	60.692
K0536	0.911	0.876	115.932	0.360	1.000	70.384	1.450	1.045	234.238	−171.944	62.294
K0537	0.907	0.914	119.019	0.329	1.000	91.303	1.495	0.920	231.940	−168.486	63.455
K0538	0.921	0.822	108.177	0.361	1.000	74.391	1.453	1.132	234.292	−169.372	64.920
K0539	0.887	0.609	92.909	0.403	1.000	66.463	1.407	1.600	234.311	−178.648	55.663
K0540	0.918	0.662	112.853	0.353	1.000	72.710	1.456	1.038	234.248	−174.959	59.289
K0541	0.899	0.692	106.280	0.370	1.000	71.631	1.389	1.193	234.347	−176.934	57.413
K0542	0.907	0.594	101.609	0.376	1.000	72.266	1.369	1.365	234.436	−168.259	66.177
K0543	0.862	0.870	112.251	0.308	1.000	105.300	1.495	1.070	228.365	−167.629	60.736
K0544	0.926	0.621	103.499	0.359	1.000	83.694	1.446	1.330	233.594	−169.451	64.144
K0545	0.877	0.642	96.039	0.416	1.000	60.100	1.327	1.466	233.351	−181.904	51.447
K0546	0.920	0.568	105.817	0.367	1.000	77.400	1.408	1.185	234.158	−170.661	63.497
K0547	0.882	0.823	110.100	0.363	1.000	72.264	1.425	1.062	234.261	−172.729	61.533
K0548	0.885	0.931	119.296	0.342	1.000	77.532	1.444	0.884	233.877	−172.256	61.622
K0549	0.905	0.784	119.686	0.338	1.000	83.686	1.428	0.914	233.254	−172.592	60.662
K0550	0.890	0.711	106.712	0.339	1.000	92.667	1.479	1.178	231.875	−169.048	62.827
K0551	0.907	0.794	115.746	0.333	1.000	86.978	1.503	0.991	232.852	−173.006	59.847
K0552	0.889	0.903	107.490	0.350	1.000	83.390	1.404	1.160	233.516	−169.052	64.463
K0553	0.921	0.798	117.378	0.353	1.000	75.817	1.460	0.965	234.083	−173.106	60.977
K0554	0.868	0.572	96.613	0.351	1.000	88.858	1.417	1.456	232.784	−169.121	63.664
K0555	0.912	0.861	124.327	0.339	1.000	80.772	1.533	0.863	233.589	−172.770	60.820
K0556	0.905	0.979	118.317	0.328	1.000	88.926	1.435	0.827	232.277	−164.747	67.529
K0557	0.876	0.911	111.071	0.308	1.000	104.955	1.510	1.031	228.444	−165.587	62.857
K0558	0.916	0.635	102.728	0.393	1.000	66.083	1.390	1.375	234.193	−174.691	59.502
K0559	0.922	0.768	108.299	0.328	1.000	95.015	1.453	1.218	231.346	−163.351	67.995
K0560	0.900	0.698	103.712	0.332	1.000	102.799	1.398	1.311	229.264	−165.338	63.926
K0561	0.902	0.586	103.399	0.330	1.000	102.986	1.447	1.344	229.244	−168.919	60.325
K0562	0.902	0.100	103.399	0.330	1.000	112.538	1.354	1.123	225.900	−164.928	60.973
K0563	0.902	0.900	103.399	0.330	1.000	97.357	1.382	1.223	230.732	−165.295	65.437

[1] B. P. Abbott, R. Abbott, T. D. Abbott, S. Abraham *et al.*, Binary black hole population properties inferred from the first and second observing runs of Advanced LIGO and Advanced Virgo, Astrophys. J. **882**, L24 (2019).

[2] B. P. Abbott, R. Abbott, T. D. Abbott, S. Abraham *et al.* (LIGO Scientific and Virgo Collaborations), Population properties of compact objects from the second LIGO–Virgo gravitational-wave transient catalog, Report No. LIGO-P2000077, 2020.

[3] LIGO Scientific, Virgo, and KAGRA Collaborations, The Population of Merging Compact Binaries Inferred Using Gravitational Waves through GWTC-3, Phys. Rev. X **13**, 011048 (2023).

[4] D. Wysocki, J. Lange, and R. O'Shaughnessy, Reconstructing phenomenological distributions of compact binaries via gravitational wave observations, Phys. Rev. D **100**, 043012 (2019).

[5] Y. Huang, C.-J. Haster, J. Roulet, S. Vitale, A. Zimmerman, T. Venumadhav, B. Zackay, L. Dai, and M. Zaldarriaga, Source properties of the lowest signal-to-noise-ratio binary black hole detections, Phys. Rev. D **102**, 103024 (2020).

[6] A. H. Nitz, C. D. Capano, S. Kumar, Y.-F. Wang, S. Kastha, M. Schäfer, R. Dhurkunde, and M. Cabero, 3-OGC: Catalog of gravitational waves from compact-binary mergers, Astrophys. J. **922**, 76 (2021).

[7] M. Boyle, D. Hemberger, D. A. B. Iozzo, G. Lovelace *et al.*, The SXS Collaboration catalog of binary black hole simulations, Classical Quantum Gravity **36**, 195006 (2019).

[8] K. Jani, J. Healy, J. A. Clark, L. London, P. Laguna, and D. Shoemaker, Georgia Tech catalog of gravitational waveforms, Classical Quantum Gravity **33**, 204001 (2016).

[9] B. Brügmann, J. A. González, M. Hannam, S. Husa, U. Sperhake, and W. Tichy, Calibration of moving puncture simulations, Phys. Rev. D **77**, 024027 (2008).

[10] B. Abbott, R. Abbott, T. Abbott, M. Abernathy *et al.*, GW150914: First results from the search for binary black hole coalescence with Advanced LIGO, Phys. Rev. D **93**, 122003 (2016).

[11] J. C. A. Miller-Jones, Astrometric observations of x-ray binaries using very long baseline interferometry, Publ. Astron. Soc. Aust. **31**, e016 (2014).

[12] B. P. Abbott, R. Abbott, T. Abbott, F. Acernese *et al.*, GW170817: Observation of Gravitational Waves from a Binary Neutron Star Inspiral, Phys. Rev. Lett. **119**, 161101 (2017).

[13] R. Abbott, T. D. Abbott, S. Abraham, F. Acernese *et al.*, Observation of gravitational waves from two neutron star–black hole coalescences, Astrophys. J. Lett. **915**, L5 (2021).

[14] LIGO Scientific Collaboration, GW190412: Observation of a binary-black-hole coalescence with asymmetric masses, Phys. Rev. D **102**, 043015 (2020).

[15] R. Abbott, T. D. Abbott, S. Abraham, and F. Acernese (LIGO Scientific Collaboration), GW190814: Gravitational waves from the coalescence of a 23 solar mass black hole with a 2.6 solar mass compact object, Astrophys. J. Lett. **896**, L44 (2020).

[16] P. Drozda, K. Belczynski, R. O'Shaughnessy, T. Bulik, and C. Fryer, Black hole-neutron star mergers: The first mass gap and kilonovae, Astron. Astrophys. **667**, A126 (2022).

[17] M. Zevin, M. Spera, C. P. L. Berry, and V. Kalogera, Exploring the lower mass gap and unequal mass regime in compact binary evolution, Astrophys. J. Lett. **899**, L1 (2020).

[18] A. Olejak, M. Fishbach, K. Belczynski, D. E. Holz, J. P. Lasota, M. C. Miller, and T. Bulik, The origin of inequality: Isolated formation of a $30+10M_{\odot}$ binary black hole merger, Astrophys. J. Lett. **901**, L39 (2020).

[19] F. S. Broekgaarden and E. Berger, Formation of the first two black hole–neutron star mergers (GW200115 and GW200105) from isolated binary evolution, Astrophys. J. Lett. **920**, L13 (2021).

[20] F. S. Broekgaarden, E. Berger, S. Stevenson, S. Justham, I. Mandel, and M. Chruślińska, Impact of massive binary star and cosmic evolution on gravitational wave observations – II. Double compact object rates and properties , Mon. Not. R. Astron. Soc. **516**, 5737 (2022).

[21] I. Mandel and A. Farmer, Merging stellar-mass binary black holes, Phys. Rep. **955**, 1 (2022).

[22] R. Narayan, T. Piran, and A. Shemi, Neutron star and black hole binaries in the galaxy, Astrophys. J. **379**, L17 (1991).

[23] K. Belczynski, V. Kalogera, and T. Bulik, A comprehensive study of binary compact objects as gravitational wave sources: Evolutionary channels, rates, and physical properties, Astrophys. J. **572**, 407 (2002).

[24] K. Belczynski, V. Kalogera, F. A. Rasio, R. E. Taam, A. Zezas, T. Bulik, T. J. Maccarone, and N. Ivanova, Compact object modeling with the StarTrack population synthesis code, Astrophys. J. Suppl. Ser. **174**, 223 (2008).

[25] K. Belczynski, S. Repetto, D. Holz, R. O'Shaughnessy, T. Bulik, E. Berti, C. Fryer, and M. Dominik, Compact binary merger rates: Comparison with LIGO/Virgo upper limits, Astrophys. J. **819**, 108 (2016).

[26] K. Belczynski, J. Klencki, C. E. Fields, A. Olejak *et al.*, Evolutionary roads leading to low effective spins, high black hole masses, and O1/O2 rates for LIGO/Virgo binary black holes, Astron. Astrophys. **636**, A104 (2020).

[27] T. Fragos *et al.*, Posydon: A general-purpose population synthesis code with detailed binary-evolution simulations, Astrophys. J. Suppl. Ser. **264**, 45 (2023).

[28] S. Stevenson and T. A. Clarke, Constraints on the contributions to the observed binary black hole population from individual evolutionary pathways in isolated binary evolution, Mon. Not. R. Astron. Soc. **517**, 4034 (2022).

[29] T. Bulik and K. Belczyński, Constraints on the binary evolution from chirp mass measurements, Astrophys. J. Lett. **589**, L37 (2003).

[30] T. Bulik, K. Belczyński, and B. Rudak, Astrophysical significance of the detection of coalescing binaries with gravitational waves, Astron. Astrophys. **415**, 407 (2004).

[31] K. W. K. Wong, K. Breivik, K. Kremer, and T. Callister, Joint constraints on the field-cluster mixing fraction, common envelope efficiency, and globular cluster radii from a population of binary hole mergers via deep learning, Phys. Rev. D **103**, 083021 (2021).

[32] M. Zevin, S. S. Bavera, C. P. L. Berry, V. Kalogera, T. Fragos, P. Marchant, C. L. Rodriguez, F. Antonini, D. E. Holz, and C. Pankow, One channel to rule them all? Constraining the origins of binary black holes using multiple formation pathways, Astrophys. J. **910**, 152 (2021).

[33] K. W. K. Wong, K. Breivik, W. M. Farr, and R. Luger, Backward population synthesis: Mapping the evolutionary history of gravitational-wave progenitors, Astrophys. J. **950**, 181 (2023).

[34] V. Gayathri, J. Healy, J. Lange, B. O'Brien, M. Szczepanczyk, I. Bartos, M. Campanelli, S. Klimenko, C. Lousto, and R. O'Shaughnessy, Eccentricity estimate for black hole mergers with numerical relativity simulations, Nat. Astron. **6**, 344 (2022).

[35] R. Gamba, M. Breschi, G. Carullo, P. Rettegno, S. Albanesi, S. Bernuzzi, and A. Nagar, GW190521: A dynamical capture of two black holes, Nat. Astron. **7**, 11 (2023).

[36] I. M. Romero-Shaw, P. D. Lasky, E. Thrane, and J. C. Bustillo, GW190521: Orbital eccentricity and signatures of dynamical formation in a binary black hole merger signal, Astrophys. J. Lett. **903**, L5 (2020).

[37] G. Fragione, A. Loeb, and F. A. Rasio, On the origin of GW190521-like events from repeated black hole mergers in star clusters, Astrophys. J. **902**, L26 (2020).

[38] R. G. Izzard, C. A. Tout, A. I. Karakas, and O. R. Pols, A new synthetic model for asymptotic giant branch stars, Mon. Not. R. Astron. Soc. **350**, 407 (2004).

[39] R. G. Izzard, L. M. Dray, A. I. Karakas, M. Lugaro, and C. A. Tout, Population nucleosynthesis in single and binary stars—I. Model, Astron. Astrophys. **460**, 565 (2006).

[40] R. G. Izzard, E. Glebbeek, R. J. Stancliffe, and O. R. Pols, Population synthesis of binary carbon-enhanced metal-poor stars, Astron. Astrophys. **508**, 1359 (2009).

[41] J. J. Eldridge, E. R. Stanway, L. Xiao, L. A. S. McClelland, G. Taylor, M. Ng, S. M. L. Greis, and J. C. Bray, Binary population and spectral synthesis version 2.1: Construction, observational verification, and new results, Publ. Astron. Soc. Aust. **34**, e058 (2017).

[42] D. Vanbeveren, E. De Donder, J. Van Bever, W. Van Rensbergen, and C. De Loore, The WR and O-type star population predicted by massive star evolutionary synthesis, New Astron. **3**, 443 (1998).

[43] D. Vanbeveren, C. De Loore, and W. Van Rensbergen, Massive stars, Astron. Astrophys. Rev. **9**, 63 (1998).

[44] J. R. Hurley, C. A. Tout, and O. R. Pols, Evolution of binary stars and the effect of tides on binary populations, Mon. Not. R. Astron. Soc. **329**, 897 (2002).

[45] M. U. Kruckow, T. M. Tauris, N. Langer, M. Kramer, and R. G. Izzard, Progenitors of gravitational wave mergers: Binary evolution with the stellar grid-based code ComBinE, Mon. Not. R. Astron. Soc. **481**, 1908 (2018).

[46] K. Breivik, S. Coughlin, M. Zevin, C. L. Rodriguez, K. Kremer, C. S. Ye, J. J. Andrews, M. Kurkowski, M. C. Digman, S. L. Larson, and F. A. Rasio, COSMIC variance in binary population synthesis, Astrophys. J. **898**, 71 (2020).

[47] N. Giacobbo, M. Mapelli, and M. Spera, Merging black hole binaries: The effects of progenitor's metallicity, mass-loss rate and Eddington factor, Mon. Not. R. Astron. Soc. **474**, 2959 (2017).

[48] V. M. Lipunov, K. A. Postnov, M. E. Prokhorov, and A. I. Bogomazov, Description of the "scenario machine", Astronomy Reports **53**, 915 (2009).

[49] M. Spera, M. Mapelli, and A. Bressan, The mass spectrum of compact remnants from the parsec stellar evolution tracks, Mon. Not. R. Astron. Soc. **451**, 4086 (2015).

[50] S. Toonen, G. Nelemans, and S. Portegies Zwart, Supernova type Ia progenitors from merging double white dwarfs—using a new population synthesis model, Astrophys. J. **546**, A70 (2012).

[51] S. Toonen, A. Hamers, and S. P. Zwart, The evolution of hierarchical triple star-systems, arXiv:1612.06172.

[52] J. W. Barrett, S. M. Gaebel, C. J. Neijssel, A. Vigna-Gómez, S. Stevenson, C. P. L. Berry, W. M. Farr, and I. Mandel, Accuracy of inference on the physics of binary evolution from gravitational-wave observations, Mon. Not. R. Astron. Soc. **477**, 4685 (2017).

[53] S. Stevenson, F. Ohme, and S. Fairhurst, Distinguishing compact binary population synthesis models using gravitational wave observations of coalescing binary black holes, Astrophys. J. **810**, 58 (2015).

[54] D. Wysocki, D. Gerosa, R. O'Shaughnessy, K. Belczynski, W. Gladysz, E. Berti, M. Kesden, and D. E. Holz, Explaining LIGO's observations via isolated binary evolution with natal kicks, Phys. Rev. D **97**, 043014 (2018).

[55] R. J. E. Smith, C. Talbot, F. Hernand ez Vivanco, and E. Thrane, Inferring the population properties of binary black holes from unresolved gravitational waves, Mon. Not. R. Astron. Soc. **496**, 3281 (2020).

[56] J. Roulet, T. Venumadhav, B. Zackay, L. Dai, and M. Zaldarriaga, Binary black hole mergers from LIGO/Virgo O1 and O2: Population inference combining confident and marginal events, Phys. Rev. D **102**, 123022 (2020).

[57] M. Zevin, C. Pankow, C. L. Rodriguez, L. Sampson, E. Chase, V. Kalogera, and F. A. Rasio, Constraining formation models of binary black holes with gravitational-wave observations, Astrophys. J. **846**, 82 (2017).

[58] Y. Bouffanais, M. Mapelli, D. Gerosa, U. N. Di Carlo, N. Giacobbo, E. Berti, and V. Baibhav, Constraining the fraction of binary black holes formed in isolation and young star clusters with gravitational-wave data, Astrophys. J. **886**, 25 (2019).

[59] S. R. Taylor and D. Gerosa, Mining gravitational-wave catalogs to understand binary stellar evolution: A new hierarchical Bayesian framework, Phys. Rev. D **98**, 083017 (2018).

[60] K. W. K. Wong and D. Gerosa, Machine-learning interpolation of population-synthesis simulations to interpret gravitational-wave observations: A case study, Phys. Rev. D **100**, 083015 (2019).

[61] J. Lange, R. O'Shaughnessy, and M. Rizzo, Rapid and accurate parameter inference for coalescing, precessing compact binaries, arXiv:1805.10457.

[62] P. Podsiadlowski, P. C. Joss, and J. J. L. Hsu, Presupernova evolution in massive interacting binaries, Astrophys. J. **391**, 246 (1992).

[63] B. Abbott, R. Abbott, T. Abbott, S. Abraham *et al.*, GWTC-1: A Gravitational-Wave Transient Catalog of Compact Binary Mergers Observed by LIGO and Virgo During the First and Second Observing Runs, Phys. Rev. X **9**, 031040 (2019).
[64] R. Abbott, T. Abbott, S. Abraham, F. Acernese *et al.*, GWTC-2: Compact Binary Coalescences Observed by LIGO and Virgo During the First Half of the Third Observing Run, Phys. Rev. X **11**, 021053 (2021).
[65] LIGO Scientific and the Virgo Collaborations *et al.*, GWTC-2.1: Deep extended catalog of compact binary coalescences observed by LIGO and Virgo during the first half of the third observing run, arXiv:2108.01045 [Phys. Rev. D (to be published)].
[66] LIGO Scientific, Virgo, and KAGRA Collaborations *et al.*, GWTC-3: Compact Binary Coalescences Observed by LIGO and Virgo During the Second Part of the Third Observing Run, arXiv:2111.03606 [Phys. Rev. X (to be published)].
[67] M. Dominik, K. Belczynski, C. Fryer, D. E. Holz, E. Berti, T. Bulik, I. Mandel, and R. O'Shaughnessy, Double compact objects. I. The significance of the common envelope on merger rates, Astrophys. J. **759**, 52 (2012).
[68] M. Dominik, K. Belczynski, C. Fryer, D. E. Holz, E. Berti, T. Bulik, I. Mandel, and R. O'Shaughnessy, Double compact objects. II. Cosmological merger rates, Astrophys. J. **779**, 72 (2013).
[69] K. Belczynski, M. Dominik, T. Bulik, R. O'Shaughnessy, C. L. Fryer, and D. E. Holz, The effect of metallicity on the detection prospects for gravitational waves, Astrophys. J. Lett. **715**, L138 (2010).
[70] K. Belczynski, D. E. Holz, T. Bulik, and R. O'Shaughnessy, The first gravitational-wave source from the isolated evolution of two stars in the 40–100 solar mass range, Nature (London) **534**, 512 (2016).
[71] W. Farr, Binary black hole population inference from gravitational wave observations, Report No. LIGO T1500562, The LIGO-Virgo-KAGRA Collaboration, 2016.
[72] I. Mandel, W. M. Farr, and J. R. Gair, Extracting distribution parameters from multiple uncertain observations with selection biases, Mon. Not. R. Astron. Soc. **486**, 1086 (2019).
[73] R. O'Shaughnessy, Notes on estimating mass distributions, Report No. LIGO T1600208, The LIGO-Virgo-KAGRA Collaboration, 2016.
[74] S. Vitale, D. Gerosa, W. M. Farr, and S. R. Taylor, Inferring the properties of a population of compact binaries in presence of selection effects, in *Handbook of Gravitational Wave Astronomy* (Springer, Singapore, 2021), pp. 1–60.
[75] M. Dominik, E. Berti, R. O'Shaughnessy, I. Mandel, K. Belczynski, C. Fryer, D. E. Holz, T. Bulik, and F. Pannarale, Double compact objects. III. Gravitational-wave detection rates, Astrophys. J. **806**, 263 (2015).
[76] K. Belczynski, A. Heger, W. Gladysz, A. J. Ruiter, S. Woosley, G. Wiktorowicz, H.-Y. Chen, T. Bulik, R. O'Shaughnessy, D. E. Holz, C. L. Fryer, and E. Berti, The effect of pair-instability mass loss on black-hole mergers, Astron. Astrophys. **594**, A97 (2016).
[77] G. Wiktorowicz, Ł. Wyrzykowski, M. Chruslinska, J. Klencki, K. A. Rybicki, and K. Belczynski, Populations of stellar-mass black holes from binary systems, Astrophys. J. **885**, 1 (2019).
[78] K. Belczynski, R. Hirschi, E. A. Kaiser, J. Liu, J. Casares, Y. Lu, R. O'Shaughnessy, A. Heger, S. Justham, and R. Soria, The formation of a $70M_{\odot}$ black hole at high metallicity, Astrophys. J. **890**, 113 (2020).
[79] R. O'Shaughnessy, C. Kim, T. Fragos, V. Kalogera, and K. Belczynski, Constraining population synthesis models via the binary neutron star population, Astrophys. J. **633**, 1076 (2005).
[80] R. O'Shaughnessy, C. Kim, V. Kalogera, and K. Belczynski, Constraining population synthesis models via observations of compact-object binaries and supernovae, Astrophys. J. **672**, 479 (2008).
[81] V. Del Favero, Constraints on compact binary formation and effective gravitational wave likelihood approximation (2022).
[82] C. L. Fryer, K. Belczynski, G. Wiktorowicz, M. Dominik, V. Kalogera, and D. E. Holz, Compact remnant mass function: Dependence on the explosion mechanism and metallicity, Astrophys. J. **749**, 91 (2012).
[83] E. E. Salpeter, The luminosity function and stellar evolution, Astrophys. J. **121**, 161 (1955).
[84] P. Kroupa, C. A. Tout, and G. Gilmore, The distribution of low-mass stars in the galactic disc, Mon. Not. R. Astron. Soc. **262**, 545 (1993).
[85] P. Kroupa and C. Weidner, Galactic-field initial mass functions of massive stars, Astrophys. J. **598**, 1076 (2003).
[86] J. Klencki, M. Moe, W. Gladysz, M. Chruslinska, D. E. Holz, and K. Belczynski, Impact of inter-correlated initial binary parameters on double black hole and neutron star mergers, Astron. Astrophys. **619**, A77 (2018).
[87] H. A. Kobulnicky and C. L. Fryer, A new look at the binary characteristics of massive stars, Astrophys. J. **670**, 747 (2007).
[88] N. Bastian, K. R. Covey, and M. R. Meyer, A universal stellar initial mass function? A critical look at variations, Annu. Rev. Astron. Astrophys. **48**, 339 (2010).
[89] G. Duchêne and A. Kraus, Stellar multiplicity, Annu. Rev. Astron. Astrophys. **51**, 269 (2013).
[90] R. O'shaughnessy, V. Kalogera, and K. Belczynski, Binary compact object coalescence rates: The role of elliptical galaxies, Astrophys. J. **716**, 615 (2010).
[91] H. Sana, S. E. de Mink, A. de Koter, N. Langer, C. J. Evans, M. Gieles, E. Gosset, R. G. Izzard, J. B. Le Bouquin, and F. R. N. Schneider, Binary interaction dominates the evolution of massive stars, Science **337**, 444 (2012).
[92] A. Olejak, C. L. Fryer, K. Belczynski, and V. Baibhav, The role of supernova convection for the lower mass gap in the isolated binary formation of gravitational wave sources, Mon. Not. R. Astron. Soc. **516**, 2252 (2022).
[93] I. Mandel and B. Müller, Simple recipes for compact remnant masses and natal kicks, Mon. Not. R. Astron. Soc. **499**, 3214 (2020).
[94] J. C. Bray and J. J. Eldridge, Neutron star kicks and their relationship to supernovae ejecta mass, Mon. Not. R. Astron. Soc. **461**, 3747 (2016).
[95] A. Vigna-Gómez, C. J. Neijssel, S. Stevenson, J. W. Barrett, K. Belczynski, S. Justham, S. E. de Mink, B. Müller, P. Podsiadlowski, M. Renzo, D. Szécsi, and I. Mandel, On the formation history of galactic double neutron stars, Mon. Not. R. Astron. Soc. **481**, 4009 (2018).

[96] J. Nordhaus, T. D. Brandt, A. Burrows, and A. Almgren, The hydrodynamic origin of neutron star kicks, Mon. Not. R. Astron. Soc. **423**, 1805 (2012).
[97] S. Rappaport, P. C. Joss, and R. F. Webbink, The evolution of highly compact binary stellar systems, Astrophys. J. **254**, 616 (1982).
[98] S. Rappaport, F. Verbunt, and P. C. Joss, A new technique for calculations of binary stellar evolution application to magnetic braking, Astrophys. J. **275**, 713 (1983).
[99] E. C. Wilson and J. Nordhaus, Convection reconciles the difference in efficiencies between low-mass and high-mass common envelopes, Mon. Not. R. Astron. Soc. **516**, 2189 (2022).
[100] J. Klencki, G. Nelemans, A. G. Istrate, and M. Chruslinska, It has to be cool: Supergiant progenitors of binary black hole mergers from common-envelope evolution, Astron. Astrophys. **645**, A54 (2021).
[101] X.-J. Xu and X.-D. Li, On the binding energy parameter λ of common envelope evolution, Astrophys. J. **716**, 114 (2010).
[102] N. Ivanova, Common envelope: On the mass and the fate of the remnant, Astrophys. J. **730**, 76 (2011).
[103] N. Ivanova and S. Chaichenets, Common envelope: Enthalpy consideration, Astrophys. J. **731**, L36 (2011).
[104] J. S. Vink, A. de Koter, and H. J. G. L. M. Lamers, Mass-loss predictions for O and B stars as a function of metallicity, Astron. Astrophys. **369**, 574 (2001).
[105] J. C. Bouret, T. Lanz, and D. J. Hillier, Lower mass loss rates in O-type stars: Spectral signatures of dense clumps in the wind of two galactic o4 stars, Astron. Astrophys. **438**, 301 (2005).
[106] J. C. Bouret, D. J. Hillier, T. Lanz, and A. W. Fullerton, Properties of galactic early-type O-supergiants: A combined FUV-UV and optical analysis, Astron. Astrophys. **544**, A67 (2012).
[107] B. Šurlan, W. R. Hamann, A. Aret, J. Kubát, L. M. Oskinova, and A. F. Torres, Macroclumping as solution of the discrepancy between H α and P v mass loss diagnostics for O-type stars, Astron. Astrophys. **559**, A130 (2013).
[108] V. Ramachandran, W. R. Hamann, L. M. Oskinova, J. S. Gallagher, R. Hainich, T. Shenar, A. A. C. Sander, H. Todt, and L. Fulmer, Testing massive star evolution, star formation history, and feedback at low metallicity. Spectroscopic analysis of OB stars in the SMC Wing, Astron. Astrophys. **625**, A104 (2019).
[109] R. Björklund, J. O. Sundqvist, J. Puls, and F. Najarro, New predictions for radiation-driven, steady-state mass-loss and wind-momentum from hot, massive stars—II. A grid of O-type stars in the galaxy and the magellanic clouds, Astrophys. J. **648**, A36 (2021).
[110] A. D. Yarovova, O. V. Egorov, A. V. Moiseev, and O. V. Maryeva, Unveiling the nitrogen-rich massive star in the metal-poor galaxy, Mon. Not. R. Astron. Soc. **518**, 2256 (2022).
[111] M. J. Rickard, R. Hainich, W.-R. Hamann, L. M. Oskinova, R. K. Prinja, V. Ramachandran, D. Pauli, H. Todt, A. A. C. Sander, T. Shenar, Y.-H. Chu, and J. S. Gallagher, Stellar wind properties of the nearly complete sample of o stars in the low metallicity young star cluster NGC 346 in the SMC galaxy, Astron. Astrophys. **666**, A189 (2022).
[112] A. C. Gormaz-Matamala, M. Curé, L. S. Cidale, and R. O. J. Venero, Self-consistent solutions for line-driven winds of hot massive stars: The m-CAK procedure, Astrophys. J. **873**, 131 (2019).
[113] A. C. Gormaz-Matamala, M. Curé, A. Lobel, J. A. Panei, J. Cuadra, I. Araya, C. Arcos, and F. Figueroa-Tapia, New self-consistent wind parameters to fit optical spectra of O-type stars observed with the HERMES spectrograph, Astron. Astrophys. **661**, A51 (2022).
[114] A. C. Gormaz-Matamala, M. Curé, D. J. Hillier, F. Najarro, B. Kubátová, and J. Kubát, New hydrodynamic solutions for line-driven winds of hot massive stars using the Lambert W-function, Astrophys. J. **920**, 64 (2021).
[115] J. O. Sundqvist, R. Björklund, J. Puls, and F. Najarro, New predictions for radiation-driven, steady-state mass-loss and wind-momentum from hot, massive stars: I. Method and first results, Astron. Astrophys. **632**, A126 (2019).
[116] J. Krtička and J. Kubát, Comoving frame models of hot star winds: II. Reduction of o star wind mass-loss rates in global models, Astron. Astrophys. **606**, A31 (2017).
[117] K. G. Gayley, J. S. Vink, A. ud Doula, A. David-Uraz, R. Ignace, R. Prinja, N. St-Louis, S. Ekström, Y. Nazé, T. Shenar, P. A. Scowen, N. Sudnik, S. P. Owocki, J. O. Sundqvist, F. A. Driessen, and L. Hennicker, Understanding structure in line-driven stellar winds using ultraviolet spectropolarimetry in the time domain, Astrophys. Space Sci. **367**, 123 (2022).
[118] P. Madau and T. Fragos, Radiation backgrounds at cosmic dawn: X-rays from compact binaries, Astrophys. J. **840**, 39 (2017).
[119] J. Zahid, G. Dima, R. Kudritzki, L. Kewley, M. Geller, H. S. Hwang, J. Silverman, and D. Kashino, The Universal relation of galactic chemical evolution: The origin of the mass–metallicity relation, Astrophys. J. **791**, 130 (2014).
[120] P. Schechter, An analytic expression for the luminosity function for galaxies, Astrophys. J. **203**, 297 (1976).
[121] A. Fontana, S. Salimbeni, A. Grazian, E. Giallongo, L. Pentericci, M. Nonino, F. Fontanot, N. Menci, P. Monaco, S. Cristiani *et al.*, The galaxy mass function up to z in the goods-music sample: Into the epoch of formation of massive galaxies, Astron. Astrophys. **459**, 745 (2006).
[122] P. A. R. Ade *et al.* (Planck Collaboration), Planck 2015 results. XIII. Cosmological parameters, Astron. Astrophys. **594**, A13 (2016).
[123] T. P. Robitaille, E. J. Tollerud, P. Greenfield *et al.* (Astropy Collaboration), Astropy: A community Python package for astronomy, Astron. Astrophys. **558**, A33 (2013).
[124] A. M. Price-Whelan, B. M. Sipőcz, H. M. Günther *et al.* (Astropy Collaboration), The Astropy project: Building an open-science project and status of the v2.0 core package, Astron. J. **156**, 123 (2018).
[125] V. Delfavero, R. O'Shaughnessy, D. Wysocki, and A. Yelikar, Compressed parametric and non-parametric approximations to the gravitational wave likelihood, arXiv:2205.14154.
[126] B. Abbott *et al.* (LIGO Scientific and Virgo Collaborations), Characterization of transient noise in Advanced LIGO relevant to gravitational wave signal GW150914, Classical Quantum Gravity **33**, 134001 (2016).

[127] B. P. Abbott, R. Abbott, T. D. Abbott, S. Abraham *et al.*, Prospects for observing and localizing gravitational-wave transients with Advanced LIGO, Advanced Virgo and KAGRA, Living Rev. Relativity **23**, 3 (2020).
[128] F. Acernese, M. Agathos, K. Agatsuma, D. Aisa *et al.*, Advanced Virgo: A second-generation interferometric gravitational wave detector, Classical Quantum Gravity **32**, 024001 (2014).
[129] B. P. Abbott, R. Abbott, and T. D. Abbott (LIGO Scientific Collaboration), Prospects for observing and localizing gravitational-wave transients with Advanced LIGO, Advanced Virgo and KAGRA, Living Rev. Relativity **23**, 3 (2020).
[130] LIGO Scientific Collaboration, LIGO Algorithm Library—LALSuite, free software (GPL) (2018).
[131] D. Wysocki and R. O'Shaughnessy, Calibrating semi-analytic VTs against reweighted injection VTs https://dcc.ligo.org/LIGO-T1800427 (2018).
[132] D. Wysocki and R. O'Shaughnessy, Bayesian parametric population models (2017), https://git.ligo.org/daniel.wysocki/bayesian-parametric-population-models.
[133] E. Berti, https://pages.jh.edu/eberti2/research/.
[134] V. Delfavero, R. O'Shaughnessy, D. Wysocki, and A. Yelikar, Normal approximate likelihoods to gravitational wave events, arXiv:2107.13082.
[135] C. K. Williams and C. E. Rasmussen, *Gaussian Processes for Machine Learning* (MIT Press, Cambridge, MA, 2006), Vol. 2.
[136] B. P. Abbott, R. Abbott, T. D. Abbott, S. Abraham, F. Acernese, K. Ackley, C. Adams, V. B. Adya *et al.* (LIGO Scientific and Virgo Collaborations), GW190521: A Binary Black Hole Merger with a Total Mass of $150M_{\odot}$, Phys. Rev. Lett. **125**, 101102 (2020).
[137] B. P. Abbott, R. Abbott, T. D. Abbott, S. Abraham, F. Acernese, K. Ackley, C. Adams, V. B. Adya *et al.* (LIGO Scientific and Virgo Collaborations), Properties and astrophysical implications of the $150M_{\odot}$ binary black hole merger GW190521, Astrophys. J. Lett. **900**, L13 (2020).
[138] K. Belczynski, The most ordinary formation of the most unusual double black hole merger, Astrophys. J. Lett. **905**, L15 (2020).
[139] C. L. Fryer, K. Belczynski, G. Wiktorowicz, M. Dominik, V. Kalogera, and D. E. Holz, Compact remnant mass function: Dependence on the explosion mechanism and metallicity, Astrophys. J. **749**, 91 (2012).
[140] P. Virtanen *et al.* (SCIPY 1.0 Contributors), SciPy 1.0: Fundamental algorithms for scientific computing in Python, Nat. Methods **17**, 261 (2020).
[141] P. Fritschel *et al.* (LIGO Scientific Collaboration), Instrument science white paper 2020, Technical Report No. LIGO-T2000407-v3, The LIGO-Virgo-KAGRA Collaboration, 2020.
[142] Y. Aso, Y. Michimura, K. Somiya, M. Ando, O. Miyakawa, T. Sekiguchi, D. Tatsumi, and H. Yamamoto (KAGRA Collaboration), Interferometer design of the KAGRA gravitational wave detector, Phys. Rev. D **88**, 043007 (2013).
[143] C. Talbot, R. Smith, E. Thrane, and G. B. Poole, Parallelized inference for gravitational-wave astronomy, Phys. Rev. D **100**, 043030 (2019).
[144] J. Sadiq, T. Dent, and D. Wysocki, Flexible and fast estimation of binary merger population distributions with adaptive KDE, Phys. Rev. D **105**, 123014 (2022).
[145] B. Edelman, F. J. Rivera-Paleo, J. D. Merritt, B. Farr *et al.*, Constraining unmodeled physics with compact binary mergers from GWTC-1, Phys. Rev. D **103**, 042004 (2021).
[146] V. Tiwari, VAMANA: Modeling binary black hole population with minimal assumptions, Classical Quantum Gravity **38**, 155007 (2021).
[147] S. Ghosh, X. Liu, J. Creighton, I. M. n. Hernandez, W. Kastaun, and G. Pratten, Rapid model comparison of equations of state from gravitational wave observation of binary neutron star coalescences, Phys. Rev. D **104**, 083003 (2021).
[148] J. Golomb and C. Talbot, Hierarchical inference of binary neutron star mass distribution and equation of state with gravitational waves, Astrophys. J. **926**, 79 (2022).
[149] F. Santoliquido, M. Mapelli, N. Giacobbo, Y. Bouffanais, and M. C. Artale, The cosmic merger rate density of compact objects: Impact of star formation, metallicity, initial mass function and binary evolution, Mon. Not. R. Astron. Soc. **502**, 4877 (2021).
[150] L. du Buisson, P. Marchant, P. Podsiadlowski, C. Kobayashi, F. B. Abdalla, P. Taylor, I. Mandel, S. E. de Mink, T. J. Moriya, and N. Langer, Cosmic rates of black hole mergers and pair-instability supernovae from chemically homogeneous binary evolution, Mon. Not. R. Astron. Soc. **499**, 5941 (2020).
[151] C. L. Rodriguez, M. Zevin, P. Amaro-Seoane, S. Chatterjee, K. Kremer, F. A. Rasio, and C. S. Ye, Black holes: The next generation—repeated mergers in dense star clusters and their gravitational-wave properties, Phys. Rev. D **100**, 043027 (2019).
[152] K. Kremer, M. Spera, D. Becker, S. Chatterjee, U. N. Di Carlo, G. Fragione, C. L. Rodriguez, C. S. Ye, and F. A. Rasio, Populating the upper black hole mass gap through stellar collisions in young star clusters, Astrophys. J. **903**, 45 (2020).
[153] B. McKernan, S. Ford, R. O'Shaughnessy, and D. Wysocki, Monte-Carlo simulations of black hole mergers in AGN disks: Low χ_{eff} mergers and predictions for LIGO, Mon. Not. R. Astron. Soc. **494**, 1203 (2020).
[154] I. Mandel, C.-J. Haster, M. Dominik, and K. Belczynski, Distinguishing types of compact-object binaries using the gravitational-wave signatures of their mergers, Mon. Not. R. Astron. Soc. **450**, L85 (2015).
[155] V. Kalogera, Spin-orbit misalignment in close binaries with two compact objects, Astrophys. J. **541**, 319 (2000).
[156] D. Gerosa, M. Kesden, E. Berti, R. O'Shaughnessy, and U. Sperhake, Resonant-plane locking and spin alignment in stellar-mass black-hole binaries: A diagnostic of compact-binary formation, Phys. Rev. D **87**, 104028 (2013).
[157] B. Abbott *et al.* (LIGO Scientific and Virgo Collaborations), Astrophysical implications of the binary black-hole merger GW150914, Astrophys. J. **818**, L22 (2016).
[158] S. Vitale, R. Lynch, R. Sturani, and P. Graff, Use of gravitational waves to probe the formation channels of compact binaries, Classical Quantum Gravity **34**, 03LT01 (2017).

[159] C. L. Rodriguez, M. Zevin, C. Pankow, V. Kalogera, and F. A. Rasio, Illuminating black hole binary formation channels with spins in Advanced LIGO, Astrophys. J. Lett. **832**, L2 (2016).
[160] S. S. Bavera, T. Fragos, Y. Qin, E. Zapartas, C. J. Neijssel, I. Mandel, A. Batta, S. M. Gaebel, C. Kimball, and S. Stevenson, The origin of spin in binary black holes, Astrophys. J. **635**, A97 (2020).
[161] W. M. Farr, N. Sravan, A. Cantrell, L. Kreidberg, C. D. Bailyn, I. Mandel, and V. Kalogera, The mass distribution of stellar-mass black holes, Astrophys. J. **741**, 103 (2011).
[162] D. Kushnir, M. Zaldarriaga, J. A. Kollmeier, and R. Waldman, Dynamical tides reexpressed, Mon. Not. R. Astron. Soc. **467**, 2146 (2017).
[163] E. O'Connor and C. D. Ott, Black hole formation in failing core-collapse supernovae, Astrophys. J. **730**, 70 (2011).
[164] M. Ugliano, H.-T. Janka, A. Marek, and A. Arcones, Progenitor-explosion connection and remnant birth masses for neutrino-driven supernovae of iron-core progenitors, Astrophys. J. **757**, 69 (2012).
[165] A. Heger, S. E. Woosley, and H. C. Spruit, Presupernova evolution of differentially rotating massive stars including magnetic fields, Astrophys. J. **626**, 350 (2005).
[166] S. Albrecht, S. Reffert, I. A. G. Snellen, and J. N. Winn, Misaligned spin and orbital axes cause the anomalous precession of DI Herculis, Nature (London) **461**, 373 (2009).
[167] S. Albrecht, J. N. Winn, G. Torres, D. C. Fabrycky, J. Setiawan, M. Gillon, E. Jehin, A. Triaud, D. Queloz, I. Snellen, and P. Eggleton, The BANANA project. V. Misaligned and precessing stellar rotation axes in CV velorum, Astrophys. J. **785**, 83 (2014).
[168] J. Abadie *et al.* (LIGO Scientific and Virgo Collaborations), Predictions for the rates of compact binary coalescences observable by ground-based gravitational-wave detectors, Classical Quantum Gravity **27**, 173001 (2010).
[169] R. O'Shaughnessy, V. Kalogera, and C. Belczynski, Short gamma-ray bursts and binary mergers in spiral and elliptical galaxies: Redshift distribution and hosts, Astrophys. J. **675**, 566 (2008).
[170] I. Mandel and R. O'Shaughnessy, Compact binary coalescences in the band of ground-based gravitational-wave detectors, Classical Quantum Gravity **27**, 114007 (2010).
[171] S. Stevenson, C. P. L. Berry, and I. Mandel, Hierarchical analysis of gravitational-wave measurements of binary black hole spin-orbit misalignments, Mon. Not. R. Astron. Soc. **471**, 2801 (2017).
[172] S. Banerjee, A. Olejak, and K. Belczynski, Symmetry breaking in merging binary black holes from young massive clusters and isolated binaries, arXiv:2302.10851.
[173] J. Fuller and L. Ma, Most black holes are born very slowly rotating, Astrophys. J. Lett. **881**, L1 (2019).
[174] K. Belczynski, C. Done, and J. P. Lasota, All apples: Comparing black holes in x-ray binaries and gravitational-wave sources, arXiv:2111.09401.
[175] D. Kushnir, M. Zaldarriaga, J. A. Kollmeier, and R. Waldman, GW150914: Spin-based constraints on the merger time of the progenitor system, Mon. Not. R. Astron. Soc. **462**, 844 (2016).
[176] A. Olejak and K. Belczynski, The implications of high black hole spins for the origin of binary black hole mergers, Astrophys. J. Lett. **921**, L2 (2021).
[177] J.-C. Bouret, F. Martins, D. J. Hillier, W. L. F. Marcolino, H. J. Rocha-Pinto, C. Georgy, T. Lanz, and I. Hubeny, Massive stars in the small magellanic cloud—evolution, rotation, and surface abundances, Astrophys. J. **647**, A134 (2021).
[178] C. Hawcroft *et al.*, X-shooting ULLYSES: Massive stars at low metallicity. III. Terminal wind speeds of ULLYSES massive stars, Astron. Astrophys. (2023), 10.1051/0004-6361/202245588
[179] K. W. K. Wong, K. Breivik, K. Kremer, and T. Callister, Joint constraints on the field-cluster mixing fraction, common envelope efficiency, and globular cluster radii from a population of binary hole mergers via deep learning, arXiv:2011.03564.
[180] S. S. Bavera, T. Fragos, M. Zevin, C. P. L. Berry, P. Marchant, J. J. Andrews, S. Coughlin, A. Dotter, K. Kovlakas, D. Misra, J. G. Serra-Perez, Y. Qin, K. A. Rocha, J. Román-Garza, N. H. Tran, and E. Zapartas, The impact of mass-transfer physics on the observable properties of field binary black hole populations, Astron. Astrophys. **647**, A153 (2021).
[181] K. Belczynski, A. Romagnolo, A. Olejak, J. Klencki, D. Chattopadhyay, S. Stevenson, M. C. Miller, J.-P. Lasota, and P. A. Crowther, The uncertain future of massive binaries obscures the origin of LIGO/Virgo sources, Astrophys. J. **925**, 69 (2022).
[182] V. Delfavero, R. O'Shaughnessy, K. Belczynski, P. Drozda, and D. Wysocki, Popsyn Models for StarTrack Inference Interpolation (1.0.0), Zenodo, 10.5281/zenodo.8161148 (2023).
[183] https://www.gw-openscience.org/.
[184] C. R. Harris, K. J. Millman, S. J. van der Walt, R. Gommers *et al.*, Array programming with NumPy, Nature (London) **585**, 357 (2020).
[185] J. D. Hunter, Matplotlib: A 2d graphics environment, Comput. Sci. Eng. **9**, 90 (2007).
[186] S. Behnel, R. Bradshaw, C. Citro, L. Dalcin, D. S. Seljebotn, and K. Smith, Cython: The best of both worlds, Comput. Sci. Eng. **13**, 31 (2011).
[187] A. Collette, *Python and HDF5* (O'Reilly, 2013).
[188] R. Pordes, D. Petravick, B. Kramer, D. Olson, M. Livny, A. Roy, P. Avery, K. Blackburn, T. Wenaus, F. Würthwein, I. Foster, R. Gardner, M. Wilde, A. Blatecky, J. McGee, and R. Quick, The open science grid, J. Phys. Conf. Ser. **78**, 012057 (2007).
[189] I. Sfiligoi, D. C. Bradley, B. Holzman, P. Mhashilkar, S. Padhi, and F. Wurthwein, The pilot way to grid resources using glideinwms, in *2009 WRI World Congress on Computer Science and Information Engineering* (IEEE, Los Angeles, CA, 2009), Vol. 2, pp. 428–432.
[190] J. D. Creighton and W. G. Anderson, *Gravitational-Wave Physics and Astronomy: An Introduction to Theory, Experiment and Data Analysis* (John Wiley & Sons, New York, 2012).